

NASA

Technical

Paper

2947

November 1989

**Fluctuating Pressures Measured
Beneath a High-Temperature,
Turbulent Boundary Layer on a
Flat Plate at a Mach Number of 5**

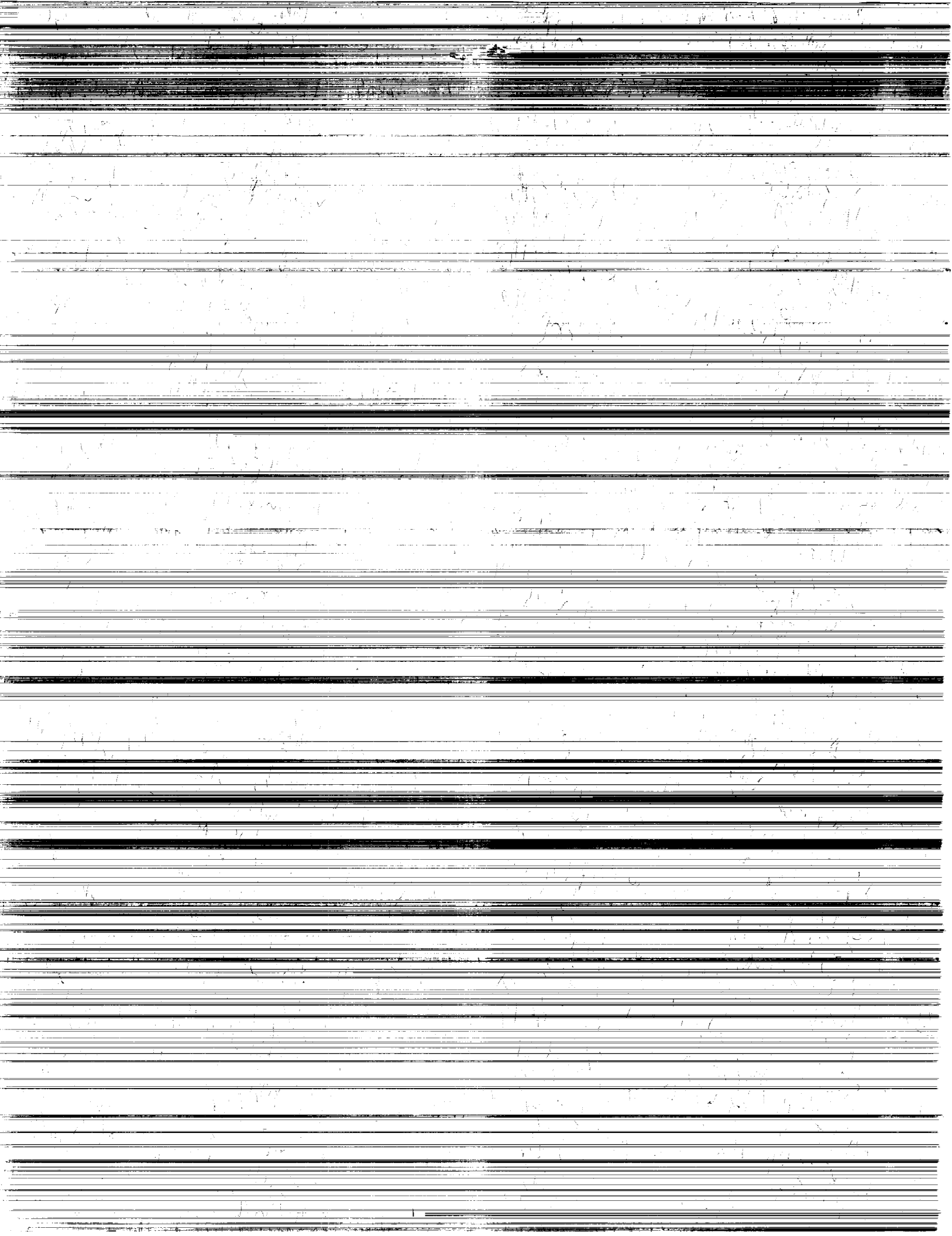
**Tony L. Parrott,
Michael G. Jones,
and Cindy W. Albertson**

**(NASA-TP-2947) FLUCTUATING PRESSURES
MEASURED BENEATH A HIGH-TEMPERATURE,
TURBULENT BOUNDARY LAYER ON A FLAT PLATE AT
MACH NUMBER OF 5 (NASA) 39 p CSCL 20A**

N90-10630

**Unclas
H1/71 0224545**

NASA



**NASA
Technical
Paper
2947**

1989

Fluctuating Pressures Measured
Beneath a High-Temperature,
Turbulent Boundary Layer on a
Flat Plate at a Mach Number of 5

Tony L. Parrott
*Langley Research Center
Hampton, Virginia*

Michael G. Jones
*PRC Kentron, Inc.
Aerospace Technologies Division
Hampton, Virginia*

Cindy W. Albertson
*Langley Research Center
Hampton, Virginia*



National Aeronautics and
Space Administration
Office of Management
Scientific and Technical
Information Division

Summary

Fluctuating pressures were measured beneath a turbulent boundary layer at a Mach number of 5 in the Langley 8-Foot High-Temperature Tunnel. The measurements were obtained from a water-cooled array of 10 sensors installed in a flat plate measuring 2.72 m by 1.31 m by 9.65 mm. The displacement-thickness Reynolds number ranged from 44.4×10^3 to 100×10^3 and was sufficiently high for natural, fully turbulent flow at the sensor locations. The nominal total temperature of the flow was 1850 K, corresponding to a total enthalpy of 2280 kJ/kg for the methane-air combustion-products test medium. Fluctuating pressure data were obtained with a digital signal acquisition system during a test run of 4 sec. The sampling rate was such that the frequency analysis could be performed up to 62.5 kHz.

A specially designed waveguide calibration system permitted in situ transfer functions of all sensors and related instrumentation to be measured. This procedure allowed an unanticipated sensor resonance to be discovered and corrected out of the digitized time histories.

Gaussian-probability density distributions describe the bulk of the pressure time history quite accurately. However, a number of pressure excursions (0.5 percent of the total data set) were observed out to absolute values of 3 to 10 times the root-mean-square (RMS) pressure. When these values were included in the probability densities, the kurtosis deviated significantly from that for a Gaussian distribution.

Total RMS pressures ranged from 0.0018 to 0.0048 times the dynamic pressure at the boundary-layer edge. For the high Reynolds number run, the power spectral densities obtained at all sensor locations (over a streamwise span of 76 mm and a cross-stream span of 29 mm) were very repeatable. Over a reduced frequency range from 0.02 (0.67 kHz) to 1.15 (38 kHz), the spectra were described approximately by a power-law roll-off with an exponent of -1.25 .

The streamwise space-time correlations exhibited the expected decaying character associated with a turbulence-generated pressure field. Convection velocities obtained from measured time delays of the correlation peaks indicated an average value of 0.87 of the free-stream velocity at the boundary-layer edge, with no apparent trend with increasing distance from the reference sensor. Because of the minimum time delay resolution of 8 μ sec and possible spurious disturbances generated by sensor misalignment, systematic errors may have been responsible for the trendless behavior of convection speed versus separation distance.

Introduction

There is a continuing need to assess aerothermal and aeroacoustic loads on the surfaces of flight vehicles that travel at hypersonic speeds. A review of aerothermal loads prediction, given by Holden in 1986 (ref. 1), indicates that recent interest in the design of transatmospheric vehicles, maneuvering re-entry vehicles, and orbital transfer vehicles has brought about an awareness that existing predictive capability is not able to support the design of such flight systems. Holden's review was directed mainly toward problems dealing with steady loads. Also of special note was the inadequacy of current prediction schemes for laminar-to-turbulent transition at hypersonic speeds. The review called attention to the severity of heat-transfer rates and gradients likely to be encountered in regions of shock/boundary-layer interaction. It was further noted that a better understanding of the steady loads problem will be coupled with an understanding of unsteady boundary-layer loads, especially for the situations involving shock/boundary-layer interaction. Finally, the unsteady loads are of intrinsic interest because of their potential to cause structural fatigue and to generate structure-borne noise and vibration. It is the unsteady or fluctuating pressure loads to which this paper is directed.

At subsonic and supersonic speeds, and at high Reynolds numbers, large portions of a vehicle surface will be exposed to attached, turbulent boundary layers that have the potential to generate large fluctuating loads. Also, in local areas of high surface curvature, such as engine inlets and control surfaces, the unsteady loads may be accentuated because of separated flow or shock/boundary-layer interaction. These loads will significantly affect the aeroshell design needed to avoid structural fatigue. Also, adverse effects of vibration on sensitive components and degradation of flight crew safety and efficiency will occur because of increased noise levels. At hypersonic speeds, the fluctuating pressure loads will become even more severe and will extend to higher frequencies. For scaled model work, these frequency components may be important out to 300 kHz. Although fluctuating pressures due to turbulent, attached boundary-layer flows have been fairly well documented for the subsonic regime, information on boundary-layer loads for supersonic and hypersonic flows is limited.

Numerous experimental investigations of subsonic boundary-layer flows have been conducted. One of the first was an investigation of turbulent pipe flow using hot wires conducted by Laufer (refs. 2 and 3) in the early 1950's. Surface-pressure

fluctuation spectra and space-time correlations for subsonic boundary-layer flow were first obtained by Willmarth (refs. 4 and 5) in the time period from 1956 to 1958. His measurements were also made inside a pipe over a Mach number range from 0.33 to 0.65 and at Reynolds numbers from 3.8×10^3 to 26×10^3 . (All Reynolds numbers are based on displacement thickness unless otherwise noted.) Willmarth reached several conclusions from this work that have been extensively referenced in the literature. First, he concluded that the root-mean-square (RMS) wall-pressure fluctuations approach 0.006 of the free-stream dynamic pressure as the ratio of sensor diameter to boundary-layer thickness approaches zero. Second, the spectra of the wall-pressure fluctuations can be cast in a dimensionless form as follows:

$$\frac{U_\infty P(\omega)}{\delta^* q_\infty^2} = f\left(\frac{\omega \delta^*}{U_\infty}\right)$$

where U_∞ denotes the free-stream velocity, $P(\omega)$ denotes the power spectral density of the pressure, δ^* denotes the boundary-layer displacement thickness, q_∞ denotes the free-stream dynamic pressure, and ω denotes the angular frequency. Finally, his space-time correlation measurements indicated a convection speed for the pressure pattern equal to about 0.82 times the free-stream velocity, at least for turbulence scales greater than 0.3 of a boundary-layer thickness δ . Also, the turbulence patterns were found to lose their identity in a distance of about 10δ .

In the mid-1960's, notable investigations were performed in wind tunnels by Bull (ref. 6) and Serafini (ref. 7). Bull conducted a test on the sidewall of a wind tunnel at Mach numbers of 0.3 and 0.5 over a Reynolds number range from 10×10^3 to 49×10^3 . He found that the RMS fluctuating pressures were about two to three times the mean wall shear stress, or 0.0045 to 0.0057 of the free-stream dynamic pressure. Serafini conducted a test on a wind-tunnel sidewall at a Mach number of 0.6 and over a Reynolds number range from 14×10^3 to 93×10^3 . He concluded that the RMS fluctuating pressure was 0.0075 of the free-stream dynamic pressure. He also confirmed that the pressure spectra could be nondimensionalized in the way that Willmarth suggested. The length scale of the pressure pattern in the streamwise direction was found to be 7.4 times that in the spanwise direction.

Richards and Mead (ref. 8) reviewed the measurements conducted at the University of Southampton, as well as at other laboratories, of wall-pressure fluctuations associated with subsonic boundary layers. They stated that the RMS pressure fluctuation has a value between two and three times the mean wall

shear stress (depending on Reynolds number), has a nearly flat frequency spectrum out to values of $\omega \delta^*/u_\infty$ of about 0.5, and falls off with increasing frequency above this value.

Measurements of fluctuating wall pressures in supersonic flows are far more sparse than in subsonic flows. A careful experiment was done by Kistler and Chen (ref. 9) in 1963 in which measurements were made on a flat plate and sidewall of a continuous-flow tunnel over a Mach number range from 1.3 to 5.0 and for a stagnation temperature of about 310 K. The Reynolds number ranged from 19×10^3 to 35×10^3 and the mean flow properties closely approximated those of equilibrium turbulent, adiabatic, flat-plate boundary layers. Measured values of the RMS fluctuating wall pressures ranged from three to five times the wall shear stress. A major effect of increasing the Mach number was to decrease the length scale of the pressure field. The convection speed of the turbulence relative to the free-stream velocity was found to decrease with increasing Mach number and to be independent of Reynolds number to within the accuracy of the measurements. The peak value of the correlation coefficient in the streamwise direction fell to one-half for a spatial separation of measuring points of about one-fifth of the boundary-layer thickness.

Speaker and Ailman (ref. 10) measured fluctuating wall pressures in turbulent boundary layers over a Mach number range from about 0.4 to 3.5. Of particular interest in this work was the inclusion of forward-facing and aft-facing steps in supersonic flow as well as the influence of a shock/boundary layer on the fluctuating pressure. As might be expected, the RMS pressures were found to be significantly higher at the front faces of steps and near the reattachment points than was the case for the flat-plate boundary layer. These pressures ranged from $0.0088q_\infty$ near the reattachment point for an aft-facing step at the lower Mach number to $0.046q_\infty$ at the face of a forward-facing step at the higher Mach number. The RMS pressure was $0.015q_\infty$ near the separation point induced by a 7.5° oblique shock wave, and it was $0.019q_\infty$ near the reattachment point.

The investigators mentioned above were aware of the spatial-averaging effects of a finite-size transducer on small-scale, convected, turbulent pressure fields. In particular, the work of Corcos (ref. 11), Willmarth and Roos (ref. 12), Corcos, Cuthbert, and Von Winkle (ref. 13), and White (ref. 14) were mainly concerned with accounting for these effects. Experimental and theoretical results from these works indicate that transducer size effects begin to effectively reduce transducer sensitivity when d/δ^* becomes greater than about 0.1 (where d denotes the

transducer diameter). Kistler and Chen (ref. 9) state that significant fluctuation energy is present out to a frequency of $5U_\infty/\delta$ (where δ denotes the boundary-layer thickness). Thus, contributions at higher frequencies will be increasingly attenuated with increasing free-stream Mach number. The measurement of these high-frequency pressure fluctuations in the hostile aerothermal environments associated with hypersonic boundary layers will require small-diameter transducers that maintain adequate sensitivity, stability, vibration insensitivity, and dynamic range.

In 1974, Raman (ref. 15) measured fluctuating pressures on a flat-plate test model exposed to hypersonic flows at Mach numbers of 5.2, 7.4, and 10.4. To measure these high-frequency pressure fluctuations, a small-diameter transducer (0.5 mm) cut from a lead-zirconate-titanate crystal was developed to operate over the frequency range from 80 to 300 kHz. Low-frequency pressure fluctuations out to about 80 kHz were measured by a commercially available piezoresistive transducer with a sensing diameter of 1.8 mm. The tunnel flow was heated to a total temperature of about 1470 K by a pebble heater. The model was exposed to this relatively high enthalpy flow for 4 sec, during which time the temperature rise of the crystal sensor was about 10 percent of the breakdown temperature of the crystal. Although these transducers are characterized by a rather high vibration sensitivity and low pressure sensitivity (typically 116 dB (re 1 V/Pa)), Raman stated that they can be successfully used with proper care in the high-enthalpy flows in this particular tunnel.

Raman found that for the range of flow parameters stated above, the RMS pressure fluctuations fall below 0.004 of the free-stream dynamic pressure (or two to three times the mean wall shear stress) and decrease with increasing dynamic pressure and Mach number. These values are considerably less than those measured by Kistler and Chen. The dependence on the Reynolds number referenced to δ^* is described approximately by $N_{Re,\delta^*}^{-0.2}$. Contributions from high-frequency components (100 to 300 kHz) were relatively small. The space-time correlations indicated a convective speed equal to 0.7 of the free-stream velocities.

The unsteady (fluctuating) pressure measurements discussed in the present paper were obtained during a more extensive test to characterize the naturally developing turbulent layer on a flat-plate model in the Langley 8-Foot High-Temperature Tunnel (8' HTT). The overall purpose of the experiment was to define conditions necessary for equilibrium turbulence for such a boundary layer and to assess

the overall quality of the turbulent boundary layer in the 8' HTT. In addition to the unsteady pressure measurements, steady pressure measurements (including surface heating rates) and total temperature and pressure measurements in the boundary layer were obtained and are reported separately (ref. 16). In the present paper, fluctuating pressure measurements are presented for a streamwise array of sensors.

Fluctuating boundary-layer pressures have been measured in various wind-tunnel environments over at least a 3-decade time span. Most of this work has been done for subsonic flows at low temperatures, on simple surface geometries, and with analog data acquisition systems. Such systems are typically limited to a dynamic range of about 40 dB and to an upper frequency range of 80 to 160 kHz. Although some effort has been directed toward improving transducer resolution by minimizing the sensitive area, little effort has been expended on extending measurement technology to high-temperature, high-speed flows.

The present study was undertaken as an initial effort in an ongoing program at the Langley Research Center to improve measurement technology and techniques for fluctuating pressure measurements in high-speed, high-temperature boundary layers. Because the project was driven by a time-limited schedule, no in-house sensor development was undertaken to achieve the small diameters used by other investigators. Instead, commercially available sensors were used that provided an acceptable compromise between important parameters such as pressure sensitivity, sensor diameter, and spurious responses to thermal and vibration inputs. The development of improved sensors is, however, in progress and will likely be available for future investigations.

In the present investigation, a square 0.15-m by 0.15-m, water-cooled, removable insert was designed to fit into the larger 2.73-m by 1.31-m flat-plate test model. Transducer mounting locations were provided in the insert for both streamwise and spanwise directions. However, only 10 data acquisition channels were available. To ensure adequate coverage in the streamwise direction to define space-time correlations, seven transducers were allotted to the streamwise direction and three to the cross-stream direction in the first part of the test series. Although the test plan included a reversal of this distribution with respect to the spanwise and cross-stream directions, facility malfunctions and tight scheduling terminated the test series prematurely. Thus, a complete data set in the cross-stream direction was not obtained.

The transducers chosen for this test were the piezoresistive, strain gauge type. The dynamic characteristics of these transducers, as specified by

the manufacturer, are limited to nominal sensitivity and resonant frequency. Previous experience has suggested that installation conditions and technique may change the frequency response. Therefore, it was deemed important to measure the in situ frequency response functions. Other calibration techniques for high-frequency pressure transducers have relied on shock waves generated in shock tubes or by high-speed projectiles to provide pressure transients as a broadband excitation source. These techniques suffer the disadvantages of little control over excitation spectrum shape, poor repeatability, and unwieldy apparatus hardware. Thus, the calibration in this experiment was accomplished via a specially designed waveguide through which broadband, plane waves were propagated. One side of the waveguide was the transducer array plate. This arrangement allowed the installed transducers to be exposed to a controlled acoustic wave field. A condenser-type microphone of known frequency response characteristics was located opposite each transducer to serve as a reference sensor. Further details of this calibration system will be described in later sections.

When the transducer array was mounted in the flat-plate test model, it was exposed to an untripped, fully turbulent boundary layer with a nominal-edge Mach number of 5. The nominal total temperature of the flow was 1850 K, corresponding to a total enthalpy of 2280 kJ/kg for the test medium of methane-air combustion products. The displacement-thickness Reynolds number ranged from 44.4×10^3 to 100×10^3 . Data were acquired and stored digitally for posttest analysis. This paper will describe this procedure, discuss typical results, and make recommendations for further investigations.

Symbols

Values are given in SI Units, but they are occasionally given in U.S. Customary Units or in both where considered useful.

C_F	local skin-friction coefficient, $2\tau_w/\rho_e U_e^2$
d	transducer diameter
f	frequency
f_{co}	cutoff frequency
$G(f), G(\omega)$	power spectral density
G_o	reference power spectral density, $(20 \mu\text{Pa}/\sqrt{\text{Hz}})^2$
g	acceleration due to gravity $(1g \approx 9.81 \text{ m/sec}^2)$

$H(\omega)$	sensor frequency response function
i	$= \sqrt{-1}$
k	number of statistical degrees of freedom
L	distance from model leading edge to sensor array plate
M_e	Mach number at boundary-layer edge
M_∞	free-stream Mach number
N	number of data points
N_B	number of data blocks
$N_{Re,L}$	Reynolds number referenced to L , $\rho_e U_e L / \mu_e$
N_{Re,δ^*}	Reynolds number referenced to δ^* , $\rho_e U_e \delta^* / \mu_e$
$N_{Re,\theta}$	Reynolds number referenced to θ , $\rho_e U_e \theta / \mu_e$
$P(n)$	discrete values of pressure time history
P_{rms}	root-mean-square pressure
$P(t)$	instantaneous pressure
P_w	static pressure at wall
$P(\omega)$	power spectral density of the pressure
q_e	dynamic pressure at boundary-layer edge
q_∞	free-stream dynamic pressure
$R(\xi, \tau)$	space-time correlation coefficient
r_T	transducer radius
T_{ad}	adiabatic wall temperature
T_w	static temperature at wall
t	time
t_B	time length of pressure time-history data block
t_{total}	total time length of pressure time-history record
U_c	convection velocity
U_e	free-stream velocity at boundary-layer edge
U_τ	wall friction velocity, $(\tau_w/\rho_w)^{1/2}$

U_{∞}	free-stream velocity
v	convection velocity
W_s	data-window correction factor
$X(\omega)$	Fourier transform of transducer excitation
$X_T(\omega)$	discrete Fourier transform of transducer excitation
x, y	Cartesian coordinates
$Y(\omega)$	Fourier transform of transducer response
z	depth of sensor recession
α	model angle of attack
α_3	skewness
α_4	kurtosis
Δ	increment
δ	boundary-layer thickness
δ^*	boundary-layer displacement thickness
θ	boundary-layer momentum thickness
μ_e	viscosity at boundary-layer edge
μ_1	mean value of pressure
μ_3	third moment of pressure probability density about mean
μ_4	fourth moment of pressure probability density about mean
ξ	separation distance
ρ_e	density at boundary-layer edge
ρ_w	density at wall
σ	variance
τ	delay time
τ_w	wall shear stress
ϕ_M	measured pressure spectra
ϕ_P	true pressure spectra
ω	angular frequency

Abbreviations:

I.D.	inner diameter
IEEE	Institute of Electrical and Electronics Engineers

mic	microphone
OASPL	overall SPL
PDF	probability density function
PSD	power spectral density
PTC	combustor total pressure
RMS	root mean square
SPL	sound pressure level, re 20 μ Pa
TTC	combustor total temperature, K
Subscript:	
calc	calculated

Facility and Apparatus

Wind-Tunnel Facility

This investigation was conducted in the Langley 8-Foot High-Temperature Tunnel (8' HTT). A schematic drawing of the facility is given in figure 1. The tunnel is a hypersonic blowdown facility that achieves a high-energy test medium by burning a mixture of methane and air under high pressure in a combustor. Combustion products are expanded to the test chamber Mach number by means of an axisymmetric, conical-contoured nozzle with an exit diameter of 2.4 m (8 ft). The nominal operating free-stream Mach number is 6.8, and pressure altitudes can be simulated between 24.4 and 36.6 km (80 000 and 120 000 ft). The gas stream in the test chamber is a free jet that enters a straight-tube supersonic diffuser where it is pumped to the atmosphere by means of a single-stage, annular air ejector. The tunnel operates at total temperatures from approximately 1300 K to 2000 K (2300°R to 3600°R), at free-stream dynamic pressures between 11.7 and 86.2 kPa (1.7 and 12.5 psia), and at free-stream unit Reynolds numbers between 0.9×10^6 and 9.0×10^6 per meter. The maximum run time is 120 sec.

The test model is stored in a pod below the test section during tunnel start-up and shutdown to minimize loads (fig. 2). Once flow conditions are established, the model is inserted into the flow on a hydraulically actuated elevator. Prior to tunnel shutdown, the model is withdrawn from the flow. As depicted in the figure, the angle of attack is set prior to the tunnel start-up. The insertion time from the edge of the flow to the tunnel centerline for the present model is typically 1.3 sec.

Boundary-Layer Survey Test Model and Sensor Array Plate

The fully instrumented, flat-plate test model installed in the Langley 8-Foot High-Temperature Tunnel is shown in figure 3. The model dimensions

are approximately 2.72 m by 1.31 m by 9.65 mm (107.3 in. by 51.5 in. by 0.38 in.). The model is fabricated from Nickel 200, which was chosen to minimize thermal gradients through the plate thickness and thermal bowing during exposure to the high-temperature stream. Estimated maximum bowing height due to thermal gradients was approximately 0.4 mm. The surface roughness of the plate was less than $0.81\text{ }\mu\text{m}$ ($32\text{ }\mu\text{in.}$). A sharp leading edge made of copper is located as shown in the photograph. For the present tests, the boundary layer was allowed to transition naturally. Three sets of boundary-layer rakes for measuring total temperature, static pressure, and total pressure distributions in the boundary layer are shown. Although not clearly visible in the photograph, the sensor array plate, used for fluctuating pressure measurements, is located as indicated. The photograph inset shows a diagram of the sensor arrangement on the array plate. A plan view of the model configuration with the array plate installed is shown in figure 4. The center of the array plate was located at the (x, y) coordinates of (2.25 m, 0.86 m), where the coordinate reference is taken as indicated in figure 4. When fluctuating pressure data were recorded, the boundary-layer rakes upstream of the array plate were removed and replaced by smooth plugs. A single set of rakes was located near the array plate at the (x, y) coordinates of (2.25 m, 0.65 m) to obtain local boundary-layer conditions. As mentioned previously, this report will be concerned exclusively with fluctuating pressure measurements obtained on the sensor array plate.

Figure 5 shows a plan view of the pressure sensor arrangement on the array plate. The sensor spacings were chosen on the basis of space-time correlations measured by previous investigators. For the present data-acquisition-system configuration, there were not sufficient instrumentation channels available to completely define both the streamwise and cross-stream spatial correlations during a single test. Thus, for the initial tests, the number of sensors was weighted in favor of the streamwise direction with the intention of locating more sensors in the cross-stream direction during the test series.

A cross-sectional view of the sensor installation is indicated in the sketch (not to scale) at the right of figure 5. It was intended that the sensors be mounted as flush as possible, with deviations (recessions) of no more than 2 percent of the sensor diameter. Misalignment estimates (recessions) are listed in figure 5 along with their ratios relative to the nominal boundary-layer thickness of 25 mm. Clearly, the desired tolerance was achieved for only 2 out of the 10 sensors. Because of time constraints on the test facility, there was not sufficient time to reconstruct

the sensor holders. Thus, the experiment was conducted with the misalignments as indicated. Coolant channels for water circulation were machined into the array plate over the length of the streamwise and cross-stream directions. The sensors were the pressure differential type with a vent I.D. of 0.25 mm. These vent tubes were connected via a manifold through a 1-m length of plastic tubing to a static pressure orifice on the array plate surface. This tubing length minimized the static pressure equalization time across the sensor diaphragms, thus avoiding large out-of-range pressure loadings on the sensor diaphragms during tunnel start-up and model insertion into the flow stream. A 1-m tube length also ensured at least 10-dB attenuation for fluctuating pressures transmitted through the tubing at the lowest frequency of interest (tube attenuation will increase with frequency), thereby allowing the sensor response to be dominated by the incident pressure.

The array plate was also equipped with two accelerometers attached to the back and one "dead-ended" sensor mount, i.e., a "blind-ended" hole such that the diaphragm was isolated from the boundary-layer flow. These precautions were taken to monitor the effects of vibration.

Pressure Sensor Selection and Installation

The chief issues in the selection of fluctuating pressure sensors were pressure sensitivity, frequency response range, sensing area diameter, electronic noise floor, and thermal and vibration sensitivity. The pressure sensors chosen were a commercially available, piezoresistive, strain gauge type with a nominal sensitivity of $18\text{ }\mu\text{V/Pa}$ (or $-95\text{ dB (re } 1\text{ V/Pa)}$), a specified diaphragm resonance of 70 kHz, and a nominal sensor diameter of 2.4 mm (0.093 in.). The sensors were temperature compensated from 300 K to 393 K with a thermal transient response of 37 Pa/K . A typical response to a $1g$ RMS acceleration is $6\text{ }\mu\text{V}$, equivalent to an output generated by a 97-dB sound pressure level. The total RMS equivalent pressure level due to broadband electronic noise is typically 83 dB over the bandwidth of 0 to 50 kHz.

The survivability of the sensor diaphragms in the presence of high heating flux was aided by water cooling the area near the sensors, the short exposure time of the test model to the flow, and the design of the sensor head. Pressure fluctuations were communicated to the diaphragm through a fine-mesh screen covering a 1-mm-diameter pinhole, of depth 1 mm, centered over the diaphragm. This overall design is believed to have provided significant protection during exposure of the sensors to the high-temperature stream. An exposure time of 6 sec limited the temperature in the vicinity of the sensors to about 310 K,

which is well within the 393-K upper compensation limit for the sensors.

The sensor diameter and diaphragm resonance were key factors in the selection of 62.5 kHz as the upper limiting frequency for the spectral analyses. A review of sensor spatial-averaging effects given by Blake (ref. 17) suggests that for the selected sensors, spatial averaging should not have attenuated the pressure signals by more than about 1 dB at 62.5 kHz. The basis for this statement is shown in figure 6 where, for this experiment, the upper limit of the parameter $\omega r_T/U_c$ was estimated to be 0.325. The two theoretical curves presented by Blake bracketed several experimental results. The nominal sensor diameter of 2.4 mm was used in this calculation, since this diameter was somewhat larger than the effective diameter of 1 mm in the discussion above concerning the sensor head structure. Thus, no correction in the spectral analysis was entered for this effect.

Data Acquisition and Reduction

Data Acquisition System

The instrumentation schematic for the fluctuating pressure measurements is shown in figure 7. Excitation and signal conditioning for the piezoresistive pressure sensors were supplied by a precision, low-noise, signal conditioning system located just outside the tunnel test chamber. The 10 channels of low-level signals from the pressure transducers were transmitted through about 10 m (33 ft) of shielded cable to the signal conditioner. Signals from the signal conditioning system were transmitted through about 41 m (135 ft) of shielded cable to the digital signal acquisition system. To help isolate the signal conditioner from power line disturbances due to switching transients of large motors located in the test area, the signal conditioning system was powered by a 24-V aircraft battery. A fixed gain at the signal conditioner could be preset by changing resistors in a feedback loop. Careful attention was given to proper grounding techniques to avoid ground loops. During a test run the system start was implemented by a contact closure located on the model actuator. Contact closure occurred when the model was 85 percent inserted into the flow (typically about 0.2 sec before the model was fully inserted into the flow).

The digital data acquisition system consisted of programmable band pass filters, transient data recorders, and a computer system as depicted in figure 7. The data recorders discretized output signals from the filters (-10 to 10 V) into 65 536 (or 2^{16}) steps. Depending on total gain selections, the pressure resolution ranged from 0.016 Pa per step to

0.043 Pa per step for a nominal sensor sensitivity of $18 \mu\text{V}/\text{Pa}$. Once started, the acquisition procedure was controlled by the computer. Data sampling rate, filter cutoff frequencies, and signal amplification were input to the program as control parameters. After a test run, data were down-loaded onto a hard disk for posttest analyses. For the present tests the data sampling rate was set at 125 kHz. The filters were operated in a band pass mode with cutoff frequencies of 100 Hz and 62.5 kHz, and the filter roll-off was 48 dB per octave. More details of the data analysis procedures will be given in the following section. A more complete description of the data acquisition system and analysis software is given by Jones (ref. 18).

Data Reduction and Analysis

Data reduction and analysis were implemented using the standard time-series-analysis procedures described in references 19 and 20. The specific software routines are given in reference 18 and will not be discussed here. However, the relevant analysis techniques, computational algorithms, and assumptions will be discussed.

The primary goal of the data analysis was to estimate pressure spectra (at the various sensor locations) and space-time correlations. The main issues of concern in the analysis are frequency resolution bandwidth, accuracy, and statistical uncertainty. As already discussed, the sensor selection was a compromise among several factors including the fluctuating pressure bandwidth, dynamic range, and test environment. One purpose of the test was to demonstrate the efficacy of digital signal acquisition technology as well as to achieve useful pressure fluctuation data. To this end a decision was made to sacrifice extended frequency bandwidth for increased sensor sensitivity. However, it was believed feasible to extend the measurements well into the frequency range affected by the sensor resonance by measuring the sensor frequency response functions. Thus, a sensor with a specified resonance of 70 kHz was chosen with the hope of acquiring useful data up to 62.5 kHz. This was the motivation for constructing the relatively elaborate waveguide calibration system indicated in the "Introduction" section. In actual fact, the procured sensors revealed resonances much lower than expected. Thus, to attain the upper frequency limit of 62.5 kHz, it was necessary to use the measured frequency response functions in their entirety, including the resonance peaks.

One advantage of the digital acquisition system is the ability to perform a "quick-look" analysis, which is useful for obtaining an immediate appraisal of data quality. This analysis consists of a visual inspection

of time history segments at selected sensors for indications of malfunction, signal clipping, or other unacceptable signal distortion. Also, probability density functions for each pressure time history can be obtained. These probability densities will be significantly non-Gaussian if a sensor resonance is present in the frequency range of interest. A quick-look analysis is available within minutes after a test run. Further analysis can be pursued or postponed, since all data are stored in a nonvolatile form. The resonance correction starts with a spectral analysis of the uncorrected data to pinpoint the resonance frequency. This correction procedure will be explained in more detail after the spectral estimation procedure is discussed.

When the corrected pressure time histories for each sensor have been recovered, the means and variances of each data block of N data points are calculated as follows:

$$\mu_1 = \frac{1}{N} \sum_{n=1}^N P(n) \quad (1)$$

$$\sigma^2 = \frac{1}{N-1} \sum_{n=1}^N [P(n) - \mu_1]^2 \quad (2)$$

In these equations $P(n)$ denotes discrete values of the pressure time history. Skewness, which measures probability-density-function asymmetry, is calculated from

$$\alpha_3 = \mu_3 / \sigma^3 \quad (3)$$

where μ_3 is the third moment of the pressure probability density about the mean. Kurtosis, which measures peakedness or flatness of the density function, is calculated from the fourth moment normalized by the fourth power of the variance; thus,

$$\alpha_4 = \mu_4 / \sigma^4 \quad (4)$$

where μ_4 is the fourth moment of the probability density about the mean. Finally, the statistical stationarity is checked by performing a "runs test" on the sequence of means and variances calculated for each of the data blocks. The runs test, described in reference 19, examines a sequence of sample means or variances taken from statistically independent blocks of data. If the sequence is trendless, i.e., randomly distributed, then the data are presumed stationary and the application of standard spectral estimation techniques allows meaningful results to be obtained. The minimum time length t_B necessary to ensure statistical independence between data blocks is estimated to be about 3 msec, based on where the autocorrelation functions approach zero. In the present

test the record length of 4 sec was divided into 128 subblocks of 32.8 msec each. Thus, it is felt that statistical independence was achieved. Also, the mean values μ_1 were essentially zero for all the data.

All spectral estimates presented in this paper are based on the finite, discrete Fourier transform of data blocks consisting of N points taken at uniform time increments of Δt seconds. Thus,

$$X_T(\omega) \approx \frac{\Delta t}{2\pi} \sum_{n=0}^{N-1} X(n \Delta t) e^{-i\omega n \Delta t} \quad (5)$$

In this equation a "boxcar" data window has been assumed that is unity over t_B and zero elsewhere. The spectral estimate is given by

$$\hat{S}_X(\omega) = W_s |X_T(\omega)|^2 \quad (6)$$

where W_s is a correction factor that accounts for the data window and experimental calibration factors. According to reference 20, subdividing a data record of time length t_{total} into N_B statistically independent data blocks, each of length t_B , allows power spectral density estimates taken from each block to be treated as a chi-square random variable with two degrees of freedom. Thus, the larger that N_B can be made, the smaller that the statistical uncertainty will be. In this investigation, N_B was chosen to be 128, and all power spectral estimates were averaged over the 128 blocks as follows:

$$\overline{\hat{S}_X(\omega)} = \frac{1}{N} \sum_{j=1}^N \hat{S}_X^j(\omega) \quad (7)$$

This procedure should yield power spectral density estimates that range from 84 percent to 115 percent of the true power spectral densities with a probability of 0.8.

The trade-off for reducing statistical uncertainty by increasing N_B is reduced frequency-resolution bandwidth of the spectral estimate for a given total time length, t_{total} . This trade-off is quantified by the equation

$$k = 2 \Delta f t_{\text{total}} \quad (8)$$

where k is the number of statistical degrees of freedom and Δf is the resolution bandwidth associated with the data block length t_B (where $\Delta f = 1/t_B$). As discussed previously, the sensor selected for this investigation had a specified resonance at 70 kHz. Thus, the analysis was set to range up to 62.5 kHz with easily correctable sensor resonance effects. This upper frequency limit of the sensor fixes the sampling rate for the data acquisition system. The total time

length of about 4 sec fixes t_{total} . The choice of 128 data blocks in turn fixes Δf at 30.5 Hz.

Space-time correlations were calculated from the corrected, discretized pressure time histories as follows:

$$R_{pp}(\xi_1, \xi_3, \tau) = \frac{\langle P(X_1, X_3, t) P(X_1 + \xi_1, X_3 + \xi_3, t + \tau) \rangle}{\langle P(X_1, X_3, t)^2 \rangle} \quad (9)$$

where $\langle \rangle$ represents a time-averaged value. The space-time correlation coefficients were obtained by normalizing the above by the appropriate standard deviations. Because the sampling time interval was 8 μsec for this particular test, the resolution of the space-time correlation peaks was not sufficient to define the convection velocities with good accuracy.

System Calibrations

Waveguide Calibrations

It was desirable to obtain the frequency response function of the complete measurement system including the installed sensors and the data acquisition and analysis system over the frequency range of interest. To accomplish this, a specially designed waveguide calibration device was built to simulate broadband "convecting" pressure disturbances moving past the sensor array and thereby exercise the complete data acquisition and analysis system with the sensors installed in the array plate. This procedure made possible the identification of any response nonuniformities or other irregularities due to instrumentation malfunction, installation technique, or "bugs" in the implementation of the analysis software. The waveguide calibration technique is believed to be superior to a shock tube calibration because of the experimental convenience and control of the spectrum shape.

A perspective view and a side view of the waveguide calibration apparatus are shown in figures 8(a) and (b), respectively. The key design feature of the apparatus is the provision for acoustic wave propagation through a rigid-walled duct with small cross-section dimensions (5 mm by 10 mm). The cross-section dimensions are chosen to be as small as practical so that only plane wave propagation is supported in the frequency range of interest. A 0.152-m length of the bottom wall of the waveguide is occupied by one leg of the transducer array, as shown in the top and bottom views of the array plate installation shown in figures 8(c) and 8(d), respectively. A 3-mm-diameter condenser microphone measures the excitation pressure for each sensor as it is successively inserted opposite each piezoresistive pressure sensor. The frequency response of the condenser microphone is uniform to within 2 dB up to 62.5 kHz.

The acoustic waves, generated by either a helium or air jet enclosed in a cylindrical chamber attached to one end of the waveguide, are absorbed into a non-reflecting termination formed by a length of plastic tubing attached to the exit end of the waveguide via a smooth square-to-round transition section. This configuration allows in situ frequency response functions of the piezoresistive sensors to be obtained up to 54 kHz, when helium is the propagating medium. These frequency response functions are used as a basis for correcting sensor resonance effects on the measured fluctuating pressure time histories.

In addition to frequency response functions, space-time correlations were measured for the broadband acoustic wave field propagating through the waveguide over the sensor array. Since the "convection speed" in this case should equal the sound speed averaged over the propagating frequencies in the waveguide, this measurement provides a check for systematic error in space-time correlation calculations.

Although it was the intention to restrict the analysis range sufficiently below the sensor resonance such that resonance would have minimal effects on the data, subsequent testing via the waveguide calibration device indicated strong resonances ranging from 30 to 40 kHz. As this would severely compromise the frequency range of the analysis, it was decided to correct across the entire resonance region to the intended upper limit of 62.5 kHz. This correction was implemented by means of the measured frequency response function for a sensor, as determined from the waveguide calibration device. The measured frequency response function for a sensor, was modeled by a single-degree-of-freedom oscillator, i.e.,

$$H(\omega) = \frac{1}{1 - \left(\frac{\omega}{\omega_o}\right)^a - 2i\zeta\left(\frac{\omega}{\omega_o}\right)} \quad (10)$$

where the exponent a , the damping factor ζ , and the resonance frequency ω_o are chosen for a best fit to the measured response. The parameter a was very nearly the ideal value of 2 for a simple, linear oscillator. Because of differences in the waveguide and tunnel test media, the sensor resonances shifted by as much as 3 kHz. Assuming that a resonance shift was the only change caused by the test environment, the sensor resonance frequency ω_o was simply changed to correspond to the resonant peak in the uncorrected spectra associated with each sensor. Thus, the corrected time history is recovered by the following inverse Fourier transform $F^{-1}(\cdot)$, i.e.,

$$P(t) = F^{-1}[X(\omega)] = F^{-1}\left[\frac{Y(\omega)}{H(\omega)}\right] \quad (11)$$

These reconstructed time histories were the basis for all the results appearing in this paper unless otherwise noted.

Waveguide Results

A typical, measured frequency response function for a sensor is shown in figure 9. This response function was obtained using helium as the waveguide medium. The magnitude is given in decibels on the left ordinate, and the phase is given in degrees on the right ordinate. The surprising feature of all "calibrations" performed in the waveguide is the prominent resonances appearing between 40 and 50 kHz (40 kHz for the sensor shown). It was initially assumed that this resonance was associated with the fundamental mode of the diaphragm and specified by the manufacturer to be 70 kHz. Discussions with the manufacturer indicated a Helmholtz resonance of the protective screen/cavity system that communicates the fluctuating pressures to the diaphragm. However, when air is used as the waveguide medium, there is no indication of a reduced resonance frequency. These observations are puzzling and have been brought to the attention of the manufacturer's technical staff with, as yet, no resolution.

It seemed prudent to expect the sensor resonance observed in the waveguide calibrator to manifest itself in the tunnel tests. Therefore, a correction algorithm was incorporated into the analysis to remove these effects from the data. This was done by fitting a single-degree-of-freedom oscillator model (eq. (10)) to the resonant feature in the uncorrected pressure spectra. The resonant frequencies in the tunnel data were shifted 4 to 5 percent from those in the calibration data. However, the general behavior is well described by the oscillator model.

Figure 10 shows a series of superimposed space-time correlations taken with 12 sensors mounted flush in the waveguide wall and with separation distances ξ of 25.4 mm (1.00 in.). In this case air is used as the propagation medium in the waveguide to provide a longer transmission time between the sensor locations. The data were taken with the same sampling rate and total record length used in the tunnel tests. Peaks in the space-time correlations for various delay times correspond to the acoustic disturbances propagating down the waveguide. The table at the upper right of the figure lists the "convection velocities" calculated between the reference (upstream) sensor and the remaining 11 downstream sensors. The table indicates a range of velocities from 318 to 343 m/sec. The average is 323 m/sec and the fractional standard deviation is 0.009. The average speed is about 6 percent lower than the free-space sound speed of 343 m/sec. This is likely due to the perturbing effect

of the sensor installation on the rigid-duct propagation speed.

Test Model Calibrations

Before each test sequence, in situ dynamic calibrations with the array plate installed in the test model were performed at 2.5 kHz at a total RMS sound pressure level (SPL) of 151 dB (690 Pa or 0.10 psi) on each of the sensors via an electromagnetic driver attached to a length of 6-mm I.D. plastic tubing. For the analysis bandwidth of 30 Hz used in this investigation, the calibration signal provided an equivalent power spectral density of 136 dB. This calibration, along with the transfer function measured in the waveguide, provides the information needed to determine absolute levels across the frequency range of interest.

Test Conditions and Procedures

The tests were conducted by starting the tunnel while the model was held out of the stream in the pod below the test section. The model was at a uniform ambient temperature (about 291 K) prior to entering the stream. Once flow conditions were established, the model was pitched to the desired angle of attack and inserted into the stream. The digital data acquisition system was started when the model reached 85 percent of full insertion, and it was allowed to record data for about 4 sec. The total time at the centerline was limited to 6 sec to avoid instrumentation damage. Figure 11(a) shows a voltage signal proportional to the model position during a typical run. The on-centerline time of 6 sec was necessary to allow all instrumentation on the survey model to stabilize. Temperature time histories obtained from a thermocouple located on the array plate are shown in figure 11(b). These plots indicate that model surface temperatures never exceeded 310 K.

The data presented in this report were taken during three test runs. The aerodynamic data pertinent to these runs are listed in table I, along with aerodynamic parameters for selected tests from other similar investigations that will be of interest for comparison purposes.

The average total temperature of the free-stream flow for the three test runs was 1850 K. The model was pitched at a 13° angle (leading edge down), producing an edge Mach number of 5. This angle of attack was necessary to produce Reynolds numbers high enough to obtain equilibrium turbulence without the use of trips, as discussed in reference 16. The Reynolds number was varied by changing the combustor total pressure, as indicated

in table I. Reynolds numbers based on flow conditions at the boundary-layer edge and distance from the leading edge to the center of the array plate ranged from 10.9×10^6 to 24.0×10^6 . Heating rates, inferred from nearby surface temperatures, ranged from 136 to 284 kW/m². Ratios of wall temperature to adiabatic wall temperature were typically 0.18. Additional parameters include surface pressure and average temperature measured at the wall of the array plate. Parameters obtained from boundary-layer rake measurements include boundary-layer edge dynamic pressure and velocity, boundary-layer thickness, displacement thickness, and momentum thickness. The skin-friction coefficient was inferred from the velocity distributions obtained from the boundary-layer rakes, as discussed in reference 16. Reynolds numbers based on displacement thickness and momentum thickness are also listed for each run.

Discussion of Results

Test Model Results

Prior to each run, an ambient spectrum was acquired with the tunnel sealed and with all associated motors disengaged. This was done to demonstrate that the noise levels measured in flow were sufficiently above the noise floor of the instrumentation. It was determined that the ambient noise levels were at least 30 dB below the minimum levels measured in the presence of flow for each of the Reynolds number test conditions.

Tunnel test conditions and relevant boundary-layer parameters for the three runs discussed in this report are listed in table I. The column labeled "Keefe" lists parameters from a previous test conducted in the same facility.¹ The last two columns list test parameters from similar investigations by Speaker and Ailman (ref. 10) and Raman (ref. 15). Results from these other investigations will be compared with the present results. As will become evident, several parameters in the table are listed for reference and will not be of direct use in the discussion that follows. Several Reynolds number parameters are listed. Of these, N_{Re,δ^*} , based on boundary-layer displacement thickness, will be most used in this report. The Reynolds number was varied by changing combustor total pressure. For the most part, only results from runs 1, 2, and 3 will be presented. These runs represent the high, low, and intermediate Reynolds number test conditions, respectively.

¹ L. Keefe conducted a similar test in the same facility in 1976 under NASA Contract NAS1-12841. The documented results of this test are unpublished.

The high Reynolds number run will be discussed first because of its consistency with similar data in the literature.

Power Spectra

Figure 12 shows a comparison of uncorrected and corrected power spectral densities on a decibel basis, obtained from a measured time history at sensor 1, for the high Reynolds number run. The data are presented over the frequency range from 0.1 to 62.5 kHz. The most prominent feature of this result is the peak appearing at about 39 kHz in the uncorrected spectrum. Spectral peaks appeared at all sensor locations at frequencies near the sensor resonances observed in the waveguide calibration tests. Furthermore, over the frequency range where this effect was obviously dominant, the spectral shapes matched closely the resonant responses as observed in the calibration spectra. This evidence provided the basis for correcting all the data to eliminate the effect of sensor resonances.

The corrected power spectral density of figure 12 is dominated by a linear trend with a negative slope from about 4 to 35 kHz. Below 4 kHz, the spectrum is dominated by a much steeper negative slope. In the corrected spectrum, a small peak corresponding to the sensor resonance is present. This is an artifact of the resonance-correction algorithm and should be ignored. Above 40 kHz, a relatively small positive slope is evident. (Note that the two linear trends meet at about 39 kHz.) This behavior at higher frequencies is probably indicative of spurious influences. In this particular case, it is believed that transducer signals at frequencies beyond 62.5 kHz were folded back or aliased into this region of the spectrum. This possibility is supported by the following three factors. First, there was evidence of a second sensor resonance above 70 kHz that was discovered from a spectral analysis performed on analog tape records of the tunnel runs. Second, the antialiasing filter roll-off was only 48 dB per octave and the cutoff was set at 62.5 kHz. Third, the sampling rate of 125 kHz was barely within the theoretical Nyquist sampling criteria at the highest frequency of interest, in contrast with the more conservative sampling rate of 2.5 times the maximum frequency of interest as generally recommended. These considerations suggest that aliasing may be responsible for the upward slope in the corrected spectrum. Consequently, all spectra presented henceforth will be truncated at 39 kHz. This truncation should eliminate any questionable data.

It is of interest to estimate the total RMS fluctuating pressure level from the corrected power spectrum of figure 12. If the dominant linear trend

is extrapolated as indicated by the dashed line, the spectrum level ranges from 102 dB at 0 Hz to 0 dB at 296 kHz. Integrating the power under this extrapolated spectrum yields 143 dB. This corresponds to 0.0011 of the dynamic free-stream pressure. This ratio is at the low end of the range reported by other investigators for subsonic and supersonic boundary-layer flow. If the region indicated by the cross-hatched area is included, the overall spectrum level is 147 dB, or 0.0018 times the free-stream dynamic pressure, which is well within the range measured by previous investigators. On the basis of these data, it is not clear whether the "extra" low-frequency contribution is from the tunnel, e.g., combustor noise, or is intrinsic to the boundary layer.

Figure 13(a) shows the superposition of spectra from streamwise sensors 1, 3, 5, and 7 for the high Reynolds number (100×10^3) run. (See run 1 in table I.) To avoid confusion, spectra from streamwise sensors 2, 4, and 6 and cross-stream sensors 8, 9, and 10 are not shown because they lie essentially on top of the curves presented. The spectra are nondimensionalized by the appropriate aerodynamic and boundary-layer parameters as suggested by Willmarth (refs. 4 and 5). (It should be noted that the dynamic pressure q_∞ in the present investigation is taken to be that at the edge of the boundary layer, which is designated as q_e in table I.) One purpose of this plot is to demonstrate the repeatability of spectra among the sensors, even to fine detail. The transfer function of the sensors varied significantly. The repeatability of these spectra confirms that the absolute calibrations, frequency response measurements, resonance-correction algorithm, and spectral-averaging process performed exceptionally well.

The shaded region in the lower part of figure 13(a) represents the range of power spectra obtained by Speaker and Ailman (ref. 10) on the wall of a blowdown-tunnel facility. These data were obtained over a streamwise span of 0.39 m at 14 sensor locations. As suggested by table I, the data were taken at a displacement-based Reynolds number that was higher by a factor of about 3.6 than that for run 1 of the present investigation. The shaded region in the upper part of figure 13(a) was taken from an investigation by Raman (ref. 15). The boundaries of this region represent the envelope of eight pressure spectra measured along a streamwise span of 29 mm. In a manner similar to that in the present test, the Raman data were obtained on a flat-plate test model with a sharp leading edge immersed in a high-enthalpy flow as indicated by the test parameters in table I. The Mach number for the Raman data was closely matched with that for the present test; however, the Reynolds number was lower by a

factor of about 4.8. It should be noted that both the Speaker and Ailman data and the Raman data extend to much higher reduced frequencies than those shown here.

One outstanding feature of the present data, in contrast with that represented by the shaded regions, is the nearly uniform power-law roll-off proportional to $\omega^{-1.25}$, as indicated by the short-dashed line that starts at a reduced frequency of 2×10^{-2} . Both the Speaker and Ailman data and the Raman data extend to higher reduced frequencies. The Speaker and Ailman data exhibit a power-law roll-off with an exponent of -5 above a reduced frequency of 3.0. In contrast, the Raman data exhibit a power-law roll-off with an exponent of -1.14 above a reduced frequency of 0.82. In the frequency range shown here, the pressure spectra from the Speaker and Ailman data exhibit significant variability compared with those of the present tests. The variability from the Raman test is much less than that of the Speaker and Ailman test, but it is still much greater than that of the present tests. There is no evidence that dynamic range limitations due to signal-to-noise ratio or spatial-averaging effects played a significant role in any of the present data. Thus, the differences between the present spectra and the Raman spectra, in particular, may be due to Reynolds number or other, as yet unknown, effects.

Figure 13(b) shows a similar plot of superimposed spectra from streamwise sensors 1, 3, 5, and 7 for the lowest Reynolds number (44.4×10^3) run. (See run 2 in table I.) Again, the same shaded regions corresponding to previous investigations, along with the power-law curve with an exponent of -1.25 , have been superimposed. The total RMS levels of these spectra are within ± 1.5 dB of that for the high Reynolds number run. The spectra do not differ substantially from those for the high Reynolds number run, as well as among themselves, except at the high frequencies. Above a reduced frequency value of 0.2, the spectra diverge and form one to two distinct peaks at various frequencies. These spectral peaks bear no obvious relation to one another, which would seem to rule out disturbances in the tunnel. Also, frequencies above the lowest sensor resonance were excluded, which rules out the peaks being associated with the sensors.

A remaining possible cause of the variability among the spectra at the higher frequencies is the small-scale turbulence generated by the misalignment of the sensor faces with the array plate surface. (See fig. 5.) The effects of sensor misalignment on measured boundary-layer turbulence spectra have been investigated by Gaudet (ref. 21) and by Hanly (ref. 22). Gaudet's measurements were limited to

subsonic boundary layers. He found that a recession depth of 5 percent of the sensor diameter can result in a 75-percent increase in the total RMS pressure relative to that for a flush-mounted sensor. Hanly measured changes in spectrum levels for supersonic free-stream Mach numbers. His results show nonuniform changes in spectrum level as a function of reduced frequency for a given recession. The spectrum level variations about a reference spectrum for the flush-mounted condition were -50 percent and -60 percent for recession values of 0.000452 δ and 0.0113 δ , respectively, at $M_\infty = 1.7$. Similar measurements at $M_\infty = 2.5$ indicated a somewhat smaller variation (-50 percent to -25 percent) about the reference spectrum for the same recessions.

It is clear from the works of Gaudet and Hanly that broadband spectral distortion due to a small sensor recession (or protrusion) can occur across the entire frequency spectrum. The sensor recessions reported in the present investigation for some of the sensors are comparable to those examined by Gaudet and Hanly. For sensors 1, 3, 5, and 7, the recessions vary from 0 to 6.4 percent of the nominal diameter, or from 0 to 0.60 percent of the nominal boundary-layer thickness. However, the spectra from these sensors show almost no variation for the high Reynolds number run, and they are in good agreement for the low Reynolds number run except in the high-frequency range. In any case, the spectrum for sensor 5, with no measurable recession, is not qualitatively different from that for sensor 1 with the largest recession. Thus, it would appear that sensor recession does not explain the spectral variability observed in the present spectra at the high frequencies as evidenced in figure 13(b).

Figure 13(c) shows another plot of superimposed spectra from the same locations for the intermediate Reynolds number (76.2×10^3) run. (See run 3 in table I.) The total RMS levels of these spectra are within ± 1.7 dB of that for the high Reynolds number run. These spectra fall somewhere between those depicted in figures 13(a) and 13(b). The primary differences between this figure and the low Reynolds number run are the diminished role of the spectral peaks and the variability from sensor to sensor at high frequencies. Otherwise, these spectra are quite repeatable and linear for a reduced frequency below about 0.2.

In general, the spectra in figure 13 show similar behavior with frequency except for unexplained peaks at the high frequencies. The total RMS levels are the same to within about ± 2 dB, which is probably within the measurement error. The Reynolds number varied by a factor of 2.25 for these data, in-

dicating that Reynolds number was not an important variable. On the other hand, the Raman data, which were taken at nominally the same Mach number in a different facility but with a similar experimental setup, produced significantly different spectra for Reynolds numbers ranging 2.2 to 4.6 times lower than those for the present tests.

Time Histories

Figure 14 shows a comparison of the uncorrected and corrected time histories for a 4-msec segment of the high Reynolds number run. The top trace is the uncorrected time history, which shows the strong periodic nature of the sensor signal resulting from the sensor resonance. The bottom trace is the "true" time history with the effects of the sensor resonance removed. Note that the fine detail is recovered which is completely masked in the uncorrected time history. Although the true spectra can apparently be reconstructed by applying this correction procedure, it is not clear that the correct phase information is recovered.

Probability Densities

Figure 15 shows the probability density distributions of the fluctuating time histories for the high, low, and intermediate Reynolds number runs, respectively, as measured at sensor 1. Various statistical parameters of interest for the distributions are listed in the figure for each run. For reference, the smooth curve represents a Gaussian distribution based on the computed means and variances. The overall sound pressure levels (OASPL) are listed as calculated from the variances. For run 1, this result was compared with that obtained by integrating the power spectrum in figure 12 and was found to be in excellent agreement. Note that the pressures on the abscissa have been normalized by the total RMS pressure or, equivalently, the standard deviation. Also, the square of the means is relatively small compared with the respective variances, thus having little effect on the RMS pressure. Skewness, which measures the distribution asymmetry, is seen to be near zero for all three runs. The kurtosis, which measures distribution peakedness, is seen to depart significantly from the value of 3.00 for a perfect Gaussian distribution.

For each run there were infrequent occurrences of pressure values with absolute values greater than $3P_{\text{rms}}$. A notable feature of all the measured distributions was the effect on the kurtosis of these outlying pressure values. (Note that for a Gaussian distribution, 99.7 percent of the distribution lies within three standard deviations of the mean.) When the kurtosis is recomputed with all pressures with an absolute value greater than $3P_{\text{rms}}$ omitted, the values

become 2.99, 2.57, and 2.98 for runs 1, 2, and 3, respectively. The fact that these new kurtosis values approach the value of 3.00, as calculated for a Gaussian distribution, is supported by a visual inspection of the deviations between the measured data and the Gaussian fit in the figure. It is clear that although these outlying pressure values constitute only about 0.5 percent of the total number of data values, they nevertheless cause a significant deviation from Gaussian behavior.

Space-Time Correlations

Figure 16 presents space-time correlations for the streamwise sensor locations and for the high Reynolds number run. The correlations were performed on the resonance-corrected time histories. The time scale has been nondimensionalized by a characteristic time. (Note that one division on this scale corresponds to a time increment of $4.8 \mu\text{sec}$.) The slope discontinuities in the correlation curves correspond to the $8\text{-}\mu\text{sec}$ time increment used in the computation (set by the sampling rate of 125 kHz). Consequently, the peaks in the correlation curves have been visually interpolated (where appropriate) to help define a correlation peak. Generally, the correlations are seen to behave in a manner characteristic of decaying, convected turbulence as has been well documented in the literature. The table in the figure includes the sensor locations, relative to sensor 1, the delay time of correlation peaks relative to sensor 1, and the convection speed ratio U_c/U_e . The convection speed ratio is seen to vary from 0.82 to 0.93, with no particular trend from the smallest to largest separations. The average value is 0.88, which is 25 percent higher than the value of 0.7 found by Raman.

The trendless behavior of the convection speed ratio with increasing sensor separation suggests a systematic error in the time delay measurements. Potential contributions to the systematic error ($\Delta U_c/U_c$) from the sensor location error ($\Delta \xi/\xi$) and time delay error ($\Delta \tau/\tau$) are indicated in figure 16. For the estimates of $\Delta \xi$ and $\Delta \tau$ indicated, the maximum combined contribution could range from 24 percent for the smallest sensor separation to 3 percent for the largest separation. This error trend is consistent with the apparent trendless behavior of the convection speed ratios.

Systematic errors can also arise because of the generation of acoustic disturbances at sensor 1, which was inadvertently recessed by 0.15 mm (or about 6 percent of the sensor diameter). Acoustic disturbances generated by such a surface discontinuity would propagate relative to the medium at sonic speed and would appear to a fixed observer as moving

at supersonic speed. This effect should become less important farther downstream because the acoustic disturbance would lose strength in proportion to the area subtended by the acoustic-disturbance Mach cone.

Another possible cause of the systematic error in the convection speed determination is the resonance-correction algorithm. Although the correction algorithm is apparently adequate for the power spectra, which are not phase dependent, it may not be adequate for the space-time correlation calculation, which is phase dependent. The phase accuracy needed for a given accuracy in convection speed determination would be dependent on sensor separation in this case also. It should be noted that the apparent convection speeds shown in figure 10, which were calculated for sound propagating in air through the waveguide, were done without the correction algorithm being incorporated. Space-time correlations with helium as the waveguide medium were also measured with similarly consistent results. In view of the questionable validity of the space-time correlations, further data of this type will not be presented.

RMS Pressure Correlations With Previous Data

The final results to be presented compare the total RMS pressures measured in this investigation with those obtained in previous investigations. Figure 17 shows a composite plot of RMS pressures, normalized by free-stream dynamic pressure, versus free-stream Mach number. (This plot was originally presented by Raman in ref. 15.) The data cover a range of Mach numbers from 0.3 to 10.5 and represent results from 16 previous investigations in a variety of test facilities. The semiempirical trends due to Houbolt and Lowson were inserted by Raman. The total RMS pressures from the high and low Reynolds number runs of the present investigation are indicated by the \oplus symbols. For completeness, the Keefe data have also been inserted.

The RMS pressures are seen to range from about $0.00071q_\infty$ to about $0.018q_\infty$, or about 28 dB. Chen's and Keefe's data are the only exceptionally high outlying data. If these data are ignored, then the RMS pressure ranges from $0.00071q_\infty$ to $0.0075q_\infty$, or about 20 dB. Note also that the Lowson estimate seems to give a better description of the trend of a large amount of the data, especially below a Mach number of 4, than the Houbolt estimate, which seems to define the upper limit of the data.

In figure 17 it is of particular interest to compare P_{rms}/q_∞ for the present test with those measured by Raman (shown by the symbols enclosed in boxes,

with arrows indicating the direction of increasing dynamic pressure). The present data also show a decrease in P_{rms}/q_∞ with increasing dynamic pressure, which is in general agreement with Raman's data. The RMS pressures for the present tests ranged from a high of $0.0048q_\infty$ to a low of $0.0018q_\infty$ for respective dynamic pressures of 108 kPa and 236 kPa.

Normalized RMS pressure measurements obtained by Keefe were well above those of the present investigation obtained in the same facility for a similar test setup. Various modifications have been made in the facility since those tests were performed. Also, the data from Keefe's test were taken at an angle of attack of 0° , compared with 13° for the present test. Nevertheless, it is of interest to compare the trends in the pressure spectrum of the high Reynolds number test (run 1) of the present investigation with the spectrum from Keefe's test. The test conditions for Keefe's data are shown in table I. Figure 18 shows a plot of these two spectra that have been normalized in the same manner as was done with Keefe's data. The shaded region is the envelope of the spectra as measured by the streamwise sensors in this investigation (as shown in fig. 13(a)). The solid-line curve is the spectrum corresponding to Keefe's data. Although the spectrum for run 1 does not cover the broad frequency covered by Keefe, the trends are seen to be generally the same. In contrast with run 1, the spectrum for Keefe's data exhibits numerous spectral spikes, which is uncharacteristic of turbulent boundary-layer pressure fluctuations. Keefe contended that these spikes were likely due to combustor resonances. Such spikes were absent from the present spectra over the analysis frequency range. Keefe's result shows large broadband contributions from a reduced frequency of about 0.002 (50 Hz) down to 0.0002 (5 Hz). This low-frequency contribution along with the spectral spikes are clearly responsible for the high RMS pressures measured by Keefe.

The final figure (fig. 19) of this discussion compares the total RMS pressure, normalized by the wall shear stress, versus the momentum-thickness-based Reynolds number for the present tests with similar data from Raman in reference 15. Raman's data are seen to cluster around a linear trend with positive slope but with significant scatter about the mean. The RMS pressure is seen to range between one to three times the wall shear stress. However, the present data indicate that P_{rms}/τ_w varies between 1.2 and 2.8. Also, only one data point from the present test is seen to fall within the trend of Raman's data. The remaining two data points fall well outside his data trend. The discrepancy between the two sets of data may result from a combination

of factors. Raman computed the momentum thickness and skin friction used in the correlation from the empirical relations given by Bies (ref. 23). For the present data, the momentum thickness and skin friction were inferred from boundary-layer rake measurements as discussed previously. As discussed by White (ref. 24), skin friction is particularly difficult to predict for compressible flows with heat transfer. White compares several theories with data and concludes that the RMS error ranges from 14 to 29 percent. This inaccuracy may also explain why these data show so much scatter.

In conclusion, the present test has yielded results similar to those obtained in previous tests in the same facility as well as in other facilities. Clearly, however, there are important differences that raise questions that cannot be answered within the limited test parameter range covered. To resolve these questions, a more comprehensive data base is needed in which both the Reynolds number and the Mach number are varied over a greater range and for different model angles of attack. Also, the spectrum analysis bandwidth needs to be extended to both lower (5 Hz) and higher (300 kHz) frequencies.

Concluding Remarks

Fluctuating pressures on the surface of a flat-plate model exposed to a high-temperature boundary layer have been measured with an array of 10 sensors in the Langley 8-Foot High-Temperature Tunnel at a Mach number of 5. The flat-plate model was set at an angle of attack of 13° to the flow, and the boundary layer at the sensor array was fully turbulent. The Reynolds number at the array varied between 44.4×10^3 and 100×10^3 , based on boundary-layer displacement thickness. Commercially available piezoresistive sensors were selected and installed in the water-cooled plate to help ensure their survival for a 6-sec exposure to the test flow. The fluctuating pressure data were acquired by a digital signal acquisition system that featured on-site, quick-look analyses in both the time and frequency domains.

Measured pressure time histories were affected by unanticipated sensor resonances between 30 and 40 kHz. However, the careful measurement of sensor transfer functions via a special waveguide calibration apparatus allowed the sensor resonance effects to be removed from the data to give apparently undistorted, digitized pressure time histories. The ability to perform on-site manipulation and analysis of large quantities of data proved indispensable for immediate appraisal of data quality. The correction procedure permitted good approximations to the true spectra to be obtained, but space-time correlations were possibly adversely affected.

Measured pressure spectra were compared with those reported by other investigators. The total root-mean-square (RMS) power obtained from integrating the power spectral density was in excellent agreement with the total RMS power obtained directly from the time history variance. Measured spectra from different sensor locations, in both streamwise and cross-stream directions, were nearly identical except at high frequencies where unexplained peaks occurred. Although these spectra differed in detail from those previously reported, the total RMS pressure levels were well within the range reported by other investigators, and the spectral variability was much less. The total RMS pressure levels ranged from 147 dB for the low Reynolds number run to 148 dB for the high Reynolds number run, or from $0.0048q_\infty$ to $0.0018q_\infty$, respectively, where q_∞ is the free-stream dynamic pressure at the boundary-layer edge. Over a reduced frequency range from 0.02 (0.67 kHz) to 1.15 (38 kHz), the spectra were described approximately by a power-law roll-off with an exponent of -1.25 .

Statistical stationarity of the pressure time histories was confirmed via the "runs test." Most of the pressure time history data (99.5 percent) were described quite accurately by a Gaussian-probability density distribution. However, a number of excursions (0.5 percent of the total data set) were observed between 3 and 10 times the root-mean-square pressure. When these values were included in the kurtosis calculation, significant deviations from a Gaussian distribution resulted.

The streamwise, space-time correlations exhibited the expected decaying character associated with a turbulence-generated pressure field. Convection velocities obtained from measured time delays of the correlation peaks indicated an average value of 0.87 of the free-stream velocity, with no apparent trend with increasing distance from the reference sensor. Because of the minimum time delay resolution of $8 \mu\text{sec}$ and possible spurious disturbances generated by sensor misalignment, systematic errors may be responsible for the trendless behavior of convection speed versus separation distance.

This work has demonstrated the efficiency and utility of modern digital signal acquisition systems coupled with high-quality instrumentation for investigating high-frequency, wall-pressure fluctuations in hypersonic boundary-layer flow. In particular, it has been shown that conventional sensors can survive a high-temperature flow environment in repeated tests, and that they can be successfully used to measure repeatable power spectra. The repeatability of these spectra confirms that the absolute calibrations, frequency response measurements, resonance-correction

algorithm, and spectral-averaging process performed exceptionally well.

It is anticipated that new technology, such as fiber optics, will allow a much-needed sensor diameter reduction to less than 1 mm and operation at elevated temperatures without sacrificing sensitivity and dynamic range. This new technology, along with advances in digital signal acquisition and processing, should enable the current data base for hypersonic boundary flows to be extended to a frequency range extending from 5 Hz to 300 kHz.

NASA Langley Research Center
Hampton, VA 23665-5225
August 30, 1989

References

1. Holden, Michael S.: A Review of Aerothermal Problems Associated With Hypersonic Flight. AIAA-86-0267, Jan. 1986.
2. Laufer, John: *Investigation of Turbulent Flow in a Two-Dimensional Channel*. NACA Rep. 1053, 1951. (Supersedes NACA TN 2123.)
3. Laufer, John: *The Structure of Turbulence in Fully Developed Pipe Flow*. NACA Rep. 1174, 1954. (Supersedes NACA TN 2954.)
4. Willmarth, William W.: Wall-Pressure Fluctuations in a Turbulent Boundary Layer. *J. Acoust. Soc. America*, vol. 28, no. 6, Nov. 1956, pp. 1048-1053.
5. Willmarth, W. W.: Space-Time Correlations of the Fluctuating Wall Pressure in a Turbulent Boundary Layer. *J. Aeronaut. Sci.*, vol. 25, no. 5, May 1958, pp. 335-336.
6. Bull, M. K.: Wall-Pressure Fluctuations Associated With Subsonic Turbulent Boundary Layer Flow. *J. Fluid Mech.*, vol. 28, pt. 4, June 22, 1967, pp. 719-754.
7. Serafini, John S.: *Wall-Pressure Fluctuations and Pressure-Velocity Correlations in a Turbulent Boundary Layer*. NASA TR R-165, 1964.
8. Richards, E. J.; and Mead, D. J., eds.: *Noise and Acoustic Fatigue in Aeronautics*. John Wiley & Sons, Ltd., 1968.
9. Kistler, A. L.; and Chen, W. S.: The Fluctuating Pressure Field in a Supersonic Turbulent Boundary Layer. *J. Fluid Mech.*, vol. 16, pt. 1, May 1963, pp. 41-64.
10. Speaker, W. V.; and Ailman, C. M.: *Spectra and Space-Time Correlations of the Fluctuating Pressures at a Wall Beneath a Supersonic Turbulent Boundary Layer Perturbed by Steps and Shock Waves*. NASA CR-486, 1966.
11. Corcos, G. M.: Resolution of Pressure in Turbulence. *J. Acoust. Soc. America*, vol. 35, no. 2, Feb. 1963, pp. 192-199.
12. Willmarth, W. W.; and Roos, F. W.: Resolution and Structure of the Wall Pressure Field Beneath a Turbulent Boundary Layer. *J. Fluid Mech.*, vol. 22, pt. 1, May 1965, pp. 81-94.
13. Corcos, G. M.; Cuthbert, J. W.; and Von Winkle, W. A.: *On the Measurement of Turbulent Pressure Fluctuations*

- With a Transducer of Finite Size.* Contract No. N-onr-222(30), Series No. 82, Issue No. 12, Univ. of California, Nov. 1959.
14. White, Pritchard H.: Effect of Transducer Size, Shape and Surface Sensitivity on the Measurement of Boundary-Layer Pressures. *J. Acoust. Soc. America*, vol. 41, no. 5, May 1967, pp. 1358-1363.
 15. Raman, K. R.: *Surface Pressure Fluctuations in Hypersonic Turbulent Boundary Layers*. NASA CR-2386, 1974.
 16. Albertson, Cindy W.: *Evaluation of Equilibrium Turbulence for a Hypersonic Boundary Layer at Nonadiabatic Wall Conditions*. M.S. Thesis, Old Dominion Univ., 1989.
 17. Blake, William K.: *Aero-Hydroacoustics for Ships, Volume II*. Rep. No. DTNSRDC-84/010, U.S. Navy, June 1984.
 18. Jones, Michael G.: *An Operations Manual for the Digital Data System*. NASA CR-181688, 1988.
 19. Bendat, Julius S.; and Piersol, Allan G.: *Random Data: Analysis and Measurement Procedures*. John Wiley & Sons, Inc., c.1971.
 20. Hardin, Jay C.: *Introduction to Time Series Analysis*. NASA RP-1145, 1986.
 21. Gaudet, L.: *The Influence of Transducer Misalignment on the Measurement of Fluctuating Surface Pressure at Low Speed*. Tech. Memo Aero 1752, British Royal Aircraft Establ., Feb. 1978.
 22. Hanly, Richard D.: Effects of Transducer Flushness on Fluctuating Surface Pressure Measurements. AIAA Paper 75-534, Mar. 1975.
 23. Bies, David Alan: *A Review of Flight and Wind Tunnel Measurements of Boundary Layer Pressure Fluctuations and Induced Structural Response*. NASA CR-626, 1966.
 24. White, Frank M.: *Viscous Fluid Flow*. McGraw-Hill, Inc., c.1974.

Table I. Aerodynamic Parameters

[Runs 1, 2, and 3 represent high, low, and intermediate Reynolds number conditions, respectively; parentheses () indicate estimated values]

Test designation	Present results			Keefe (unpublished)	Speaker and Ailman (ref. 10)	Raman (ref. 15)
	Run 1	Run 2	Run 3			
PTC, kPa	22620	10340	17240	17120	726	786
TTC, K	1810	1860	1870	1610	292	932
α , deg	13	13	13	0	(a)	0
M_e	4.92	4.96	4.88	6.15	3.45	5.20
U_e , m/sec	1850	1850	1890	1710	643	1340
q_e , kPa	236	108	181	59	83	35
P_w , kPa	14.6	6.45	11.4	2.32	10.4	1.03
$\tau_{w,calc}$, Pa	361	184	290	(127)	70	(67)
T_w , K	300	296	299	(300)	(292)	(300)
δ , mm	25.4	24.6	26.2	10.1	20.6	(13.2)
δ^* , mm	9.40	9.17	9.47	10.07	8.39	(7.26)
θ , mm	1.55	1.60	1.66	1.89	1.25	(0.59)
$C_{F,calc} \times 10^{-3}$	1.53	1.70	1.60	(3.3)	0.85	(1.90)
$N_{Re,L} \times 10^6$	24	10.9	18.1	3.33	^b 42.5	2.1
$N_{Re,\delta^*} \times 10^3$	100	44.4	76.2	25.7	357	(20.9)
$N_{Re,\theta} \times 10^3$	16.5	7.76	13.3	4.8	53.2	(1.7)
$U_{\tau,calc}$, m/sec	48.3	51.1	50.0	(69.4)	(24.1)	(75.0)
P_{rms} , Pa	436	517	360	718	149	135

^aData obtained on tunnel sidewall.

^bUnit Reynolds number per meter.

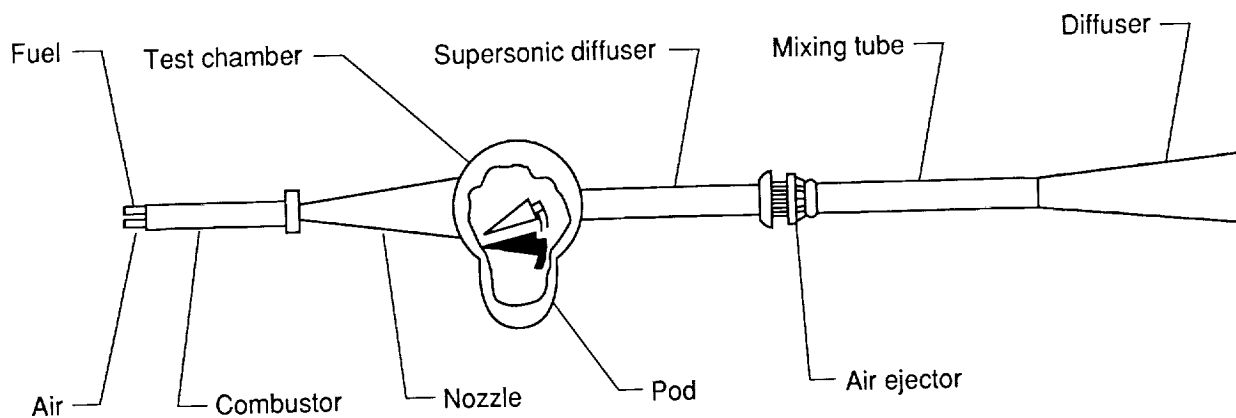


Figure 1. Schematic of the Langley 8-Foot High-Temperature Tunnel.

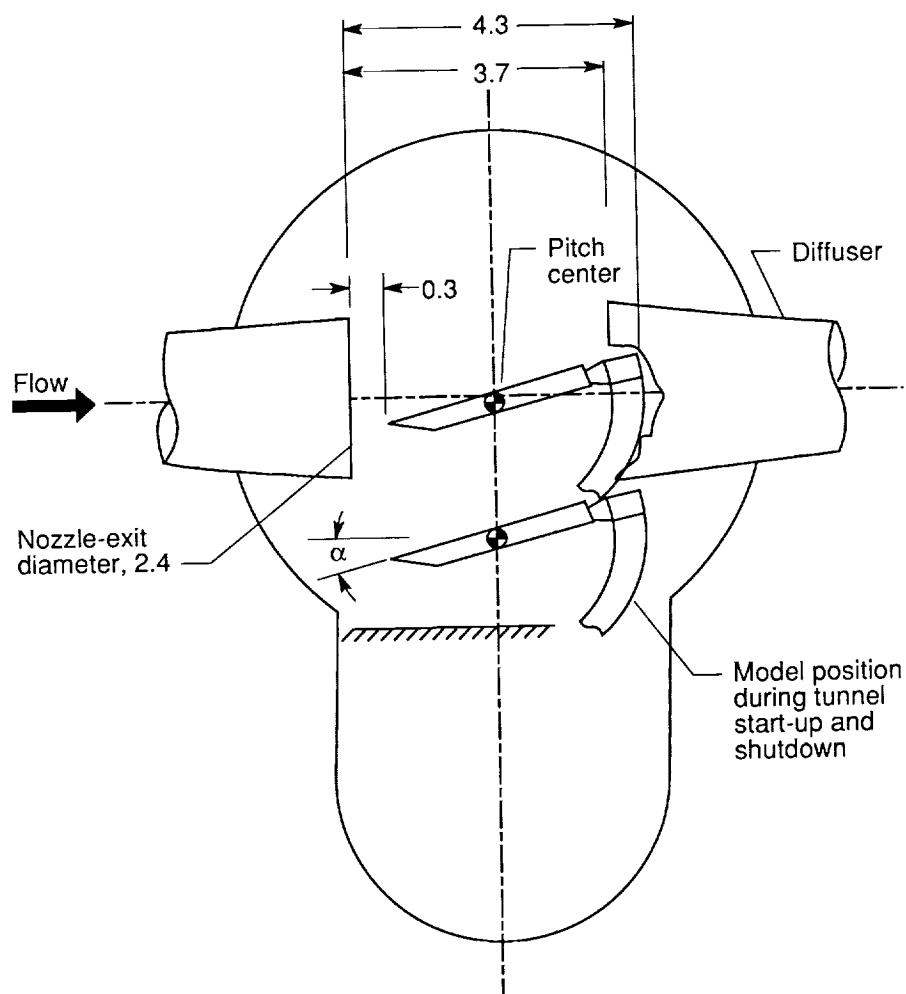
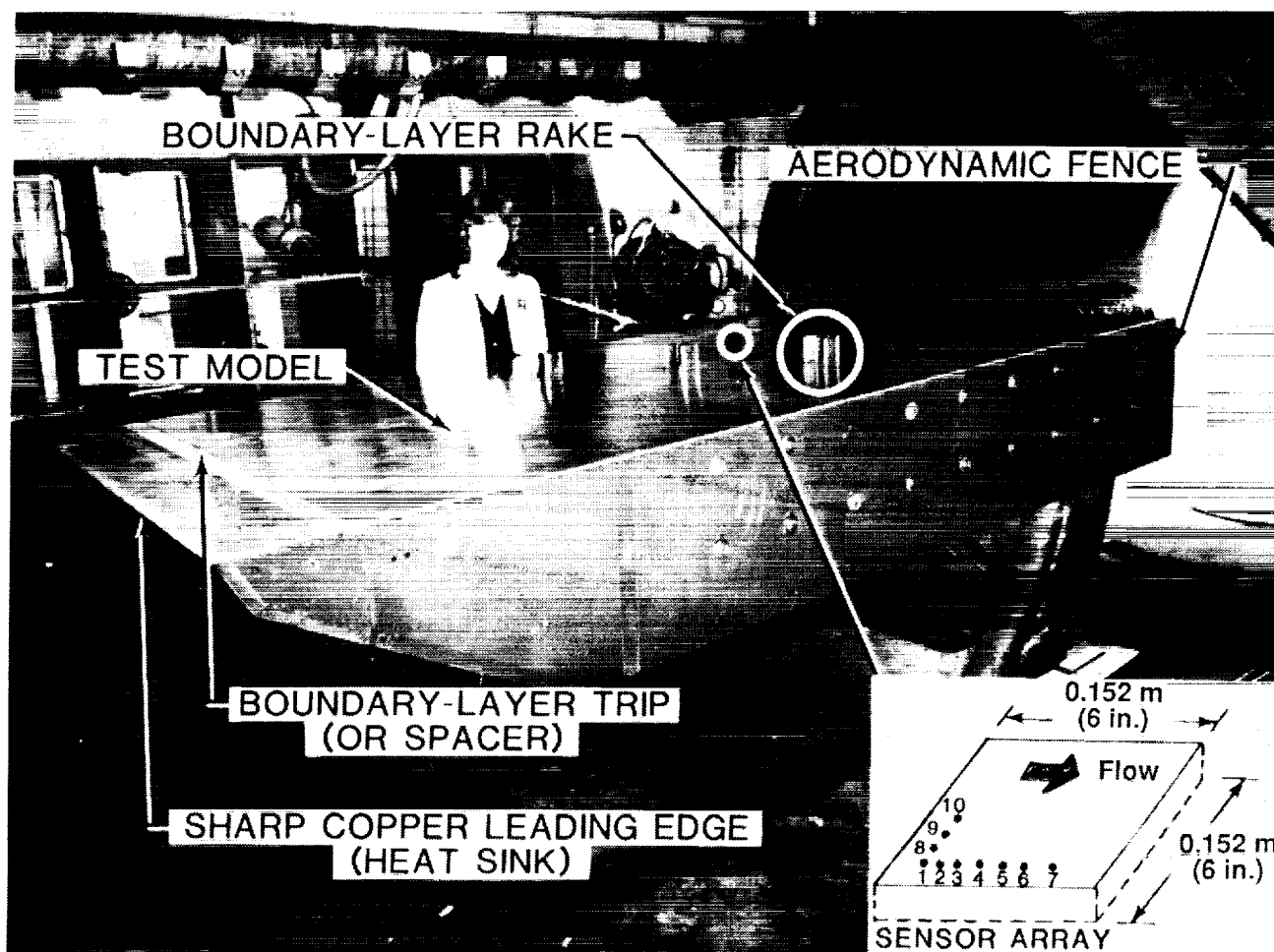


Figure 2. Cross-sectional view of test section of the Langley 8-Foot High-Temperature Tunnel. All dimensions are given in meters.



L-88-3992

Figure 3. Test model installed in tunnel with sensor array location indicated.

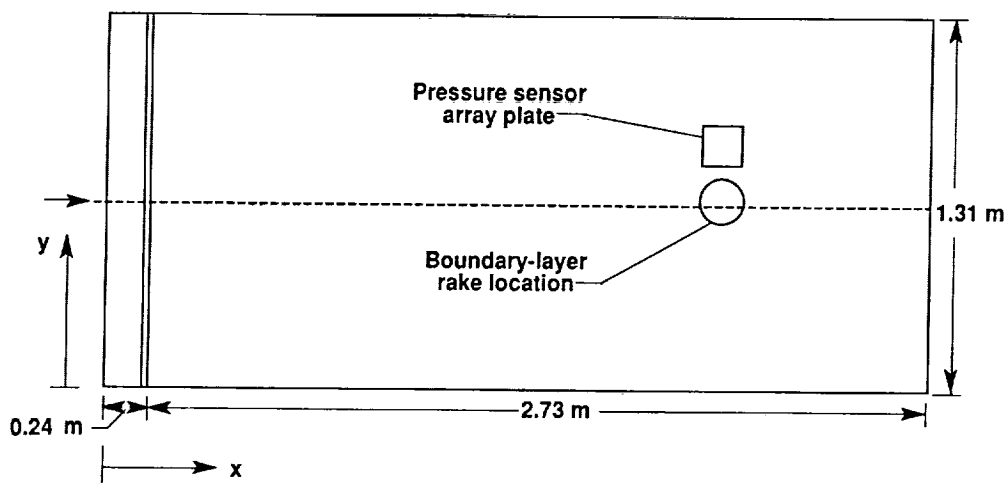


Figure 4. Pressure sensor array plate and boundary-layer rake locations on test model.

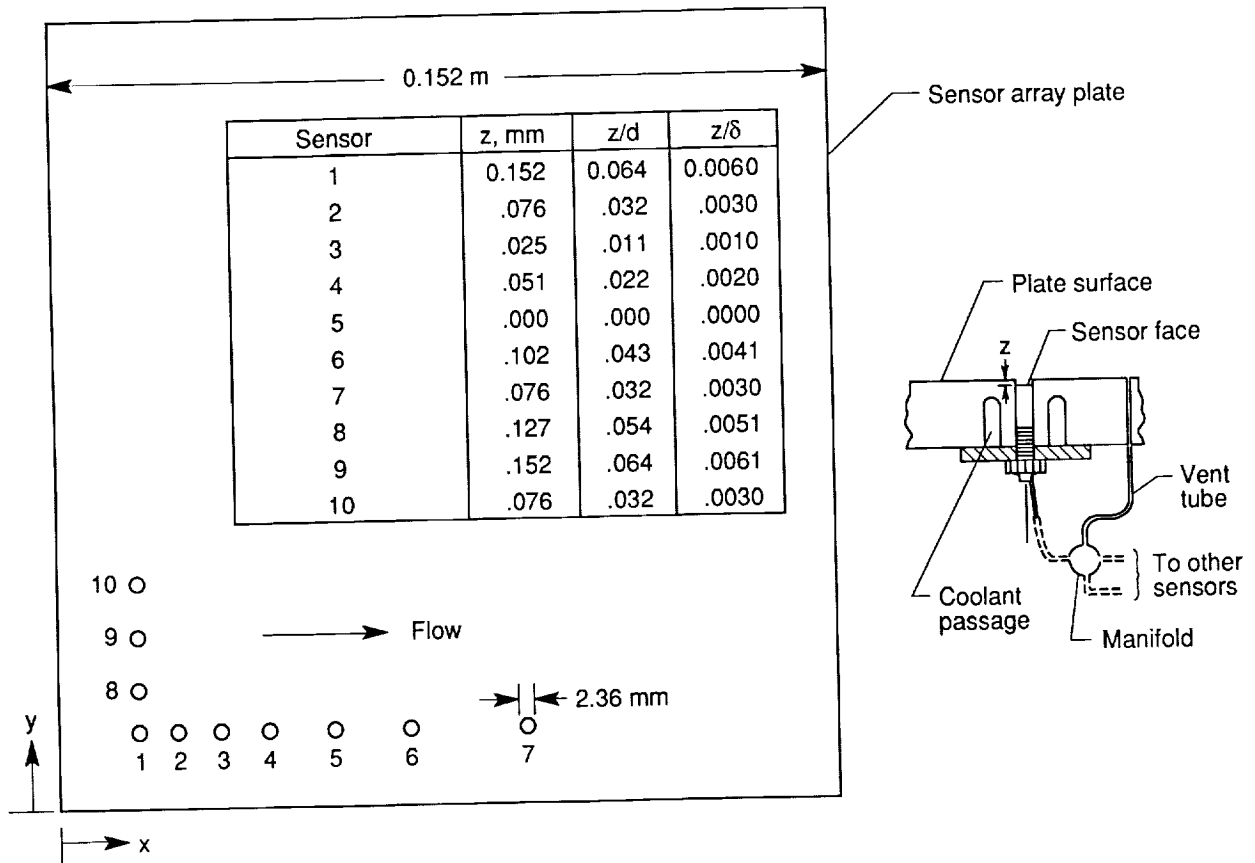


Figure 5. Plan view of sensor locations on array plate and schematic of sensor installation.

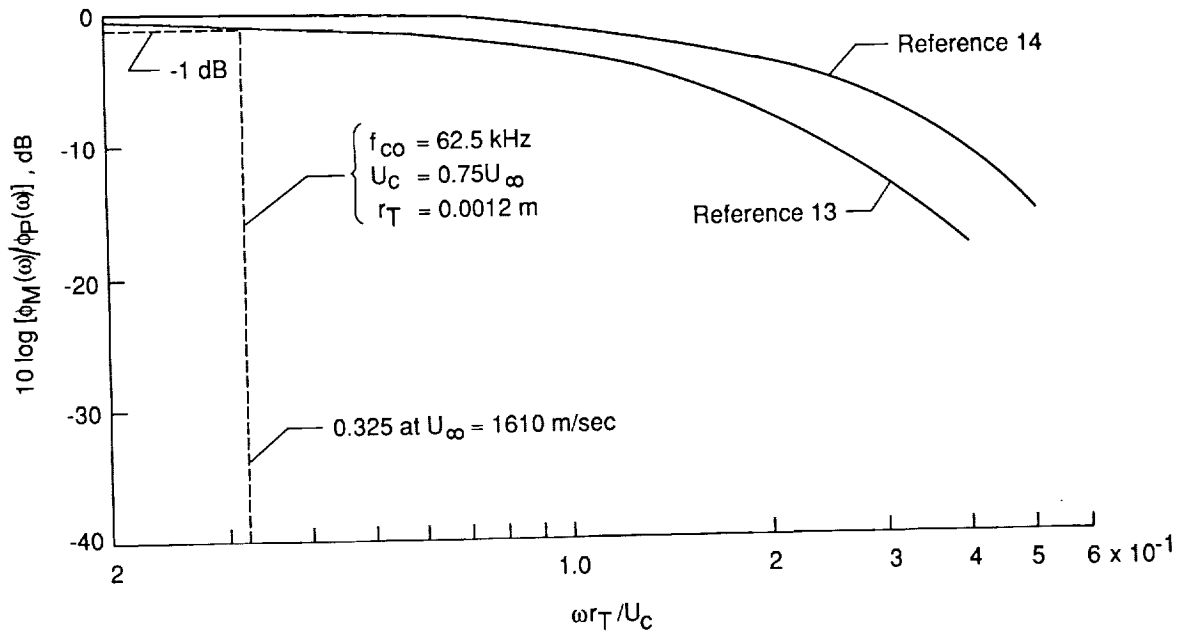


Figure 6. Theoretical estimates of spatial-averaging effect on boundary-layer, wall pressure spectra from Blake (ref. 17, p. 778).

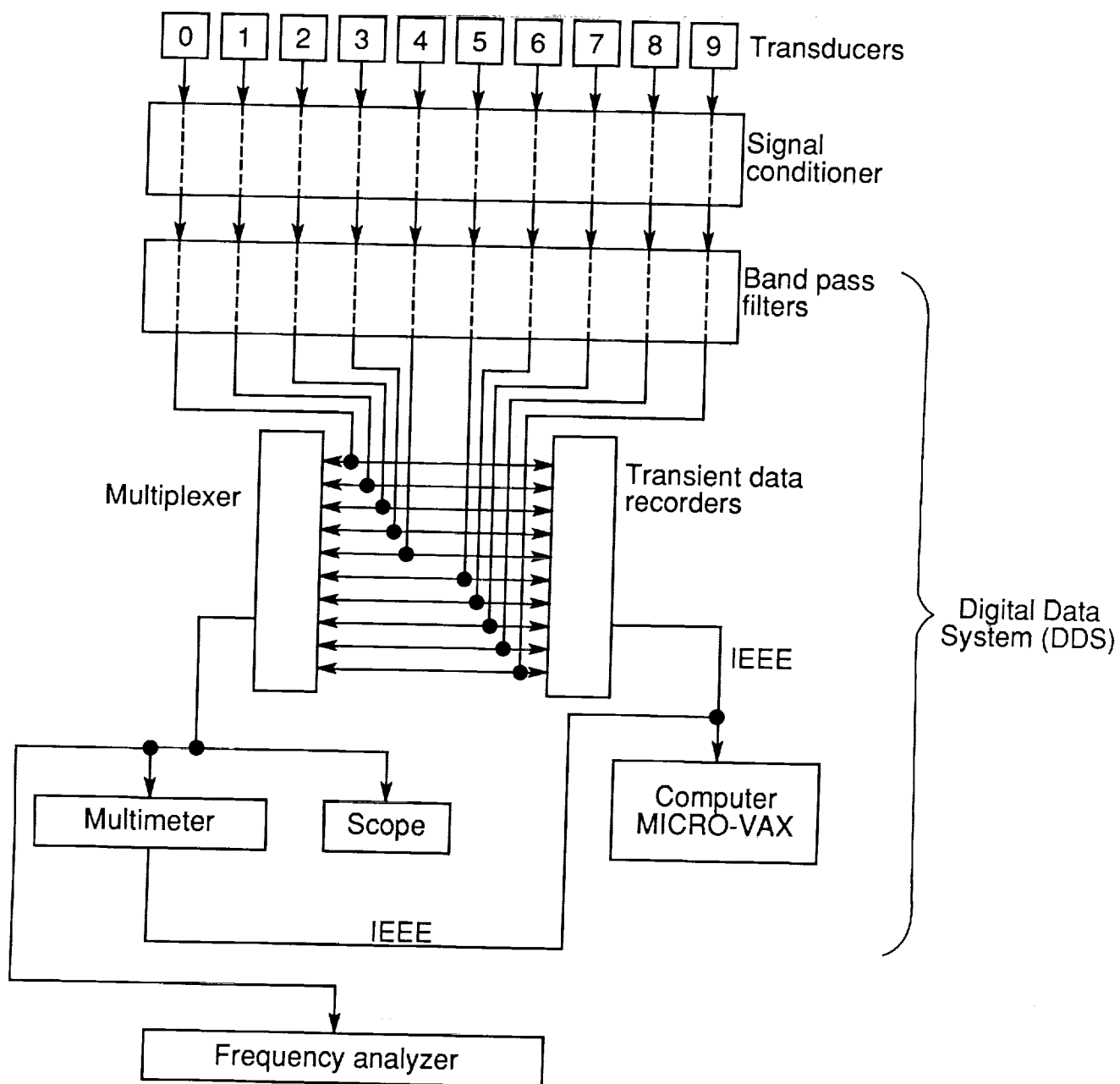
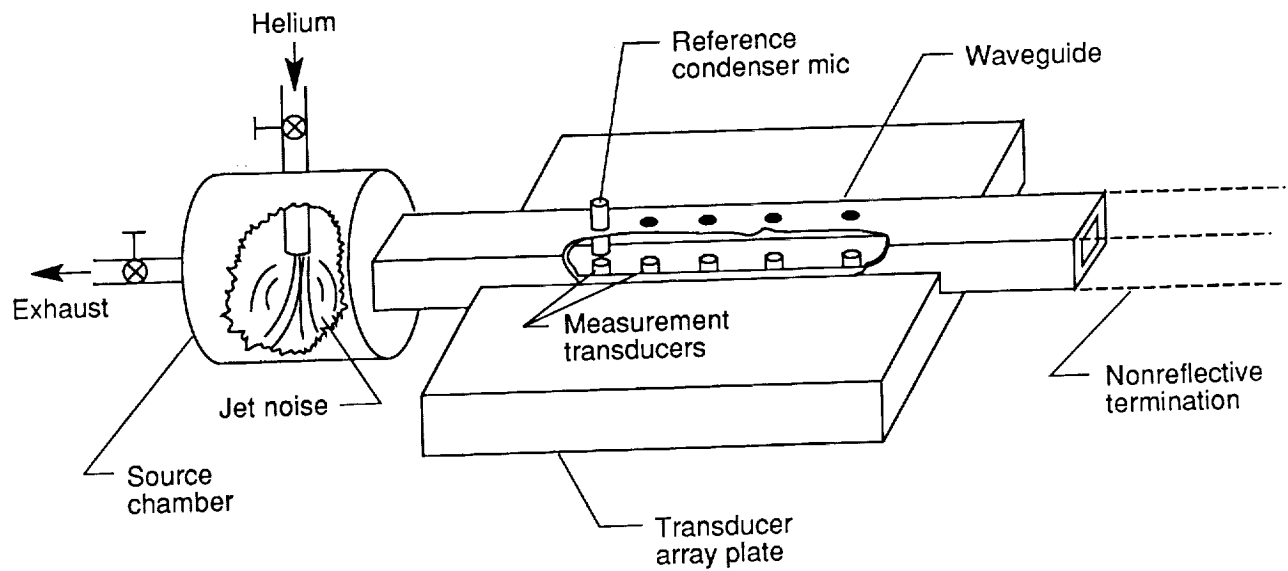
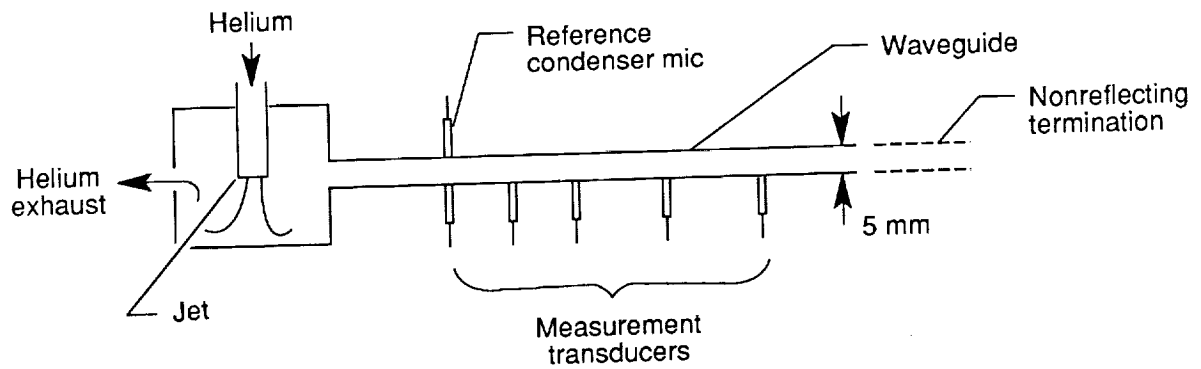


Figure 7. Instrumentation schematic.

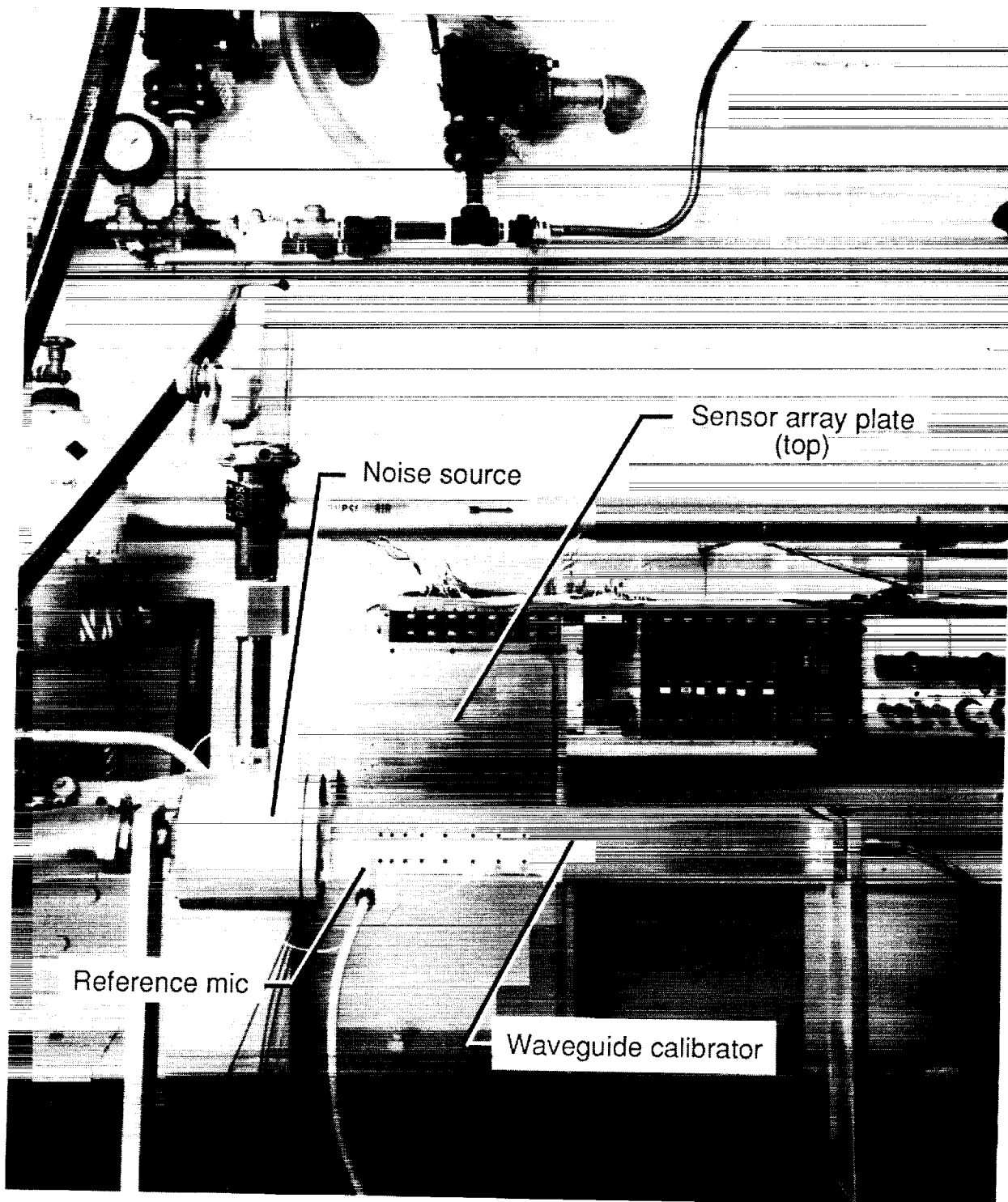


(a) Perspective view.



(b) Side view.

Figure 8. Waveguide calibration system.

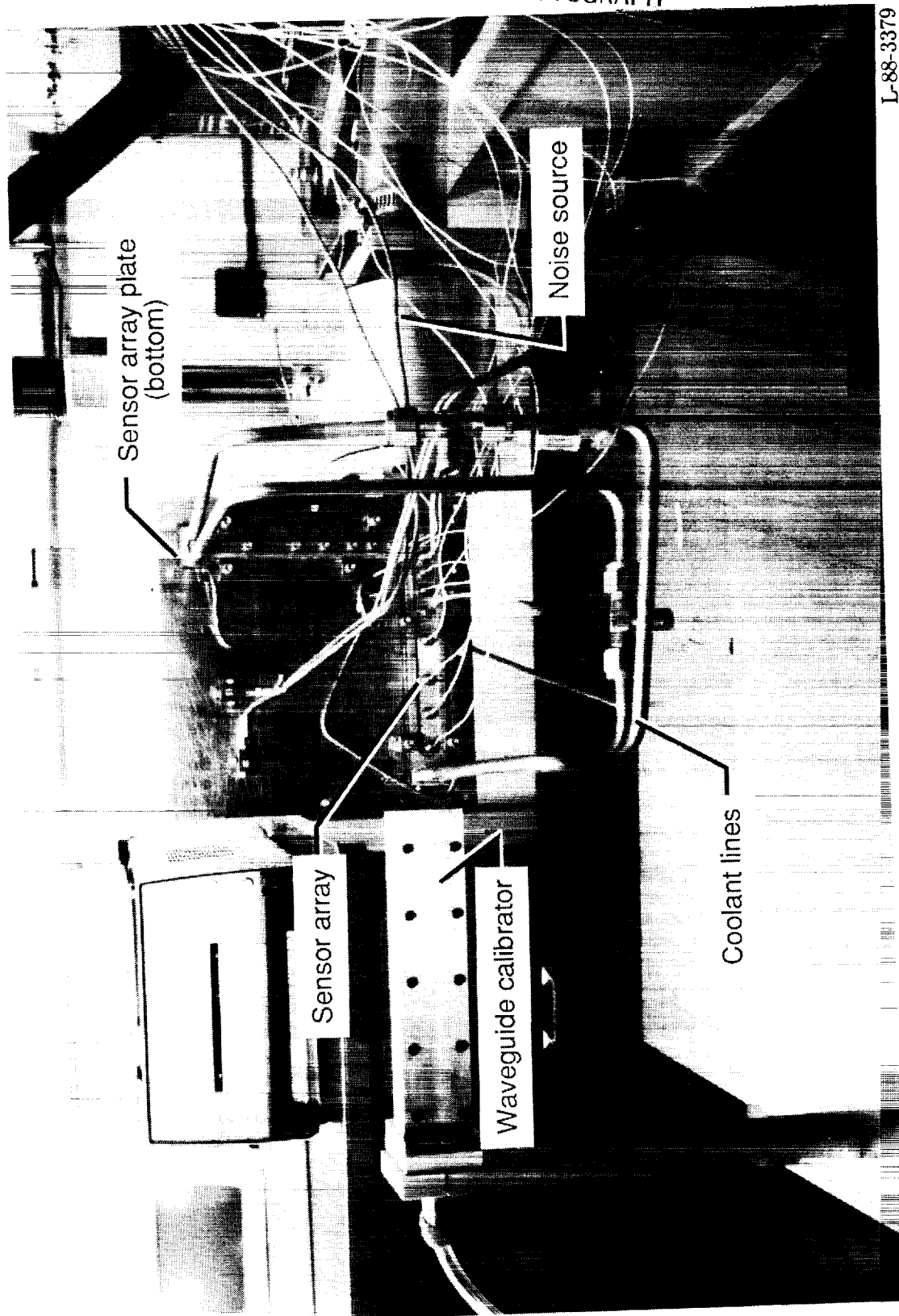


L-88-2377

(c) Top view of sensor array plate installed in waveguide calibrator.

Figure 8. Continued.

ORIGINAL PAGE
BLACK AND WHITE PHOTOGRAPH



(d) Bottom view of sensor array plate installed in waveguide calibrator.

Figure 8. Concluded.

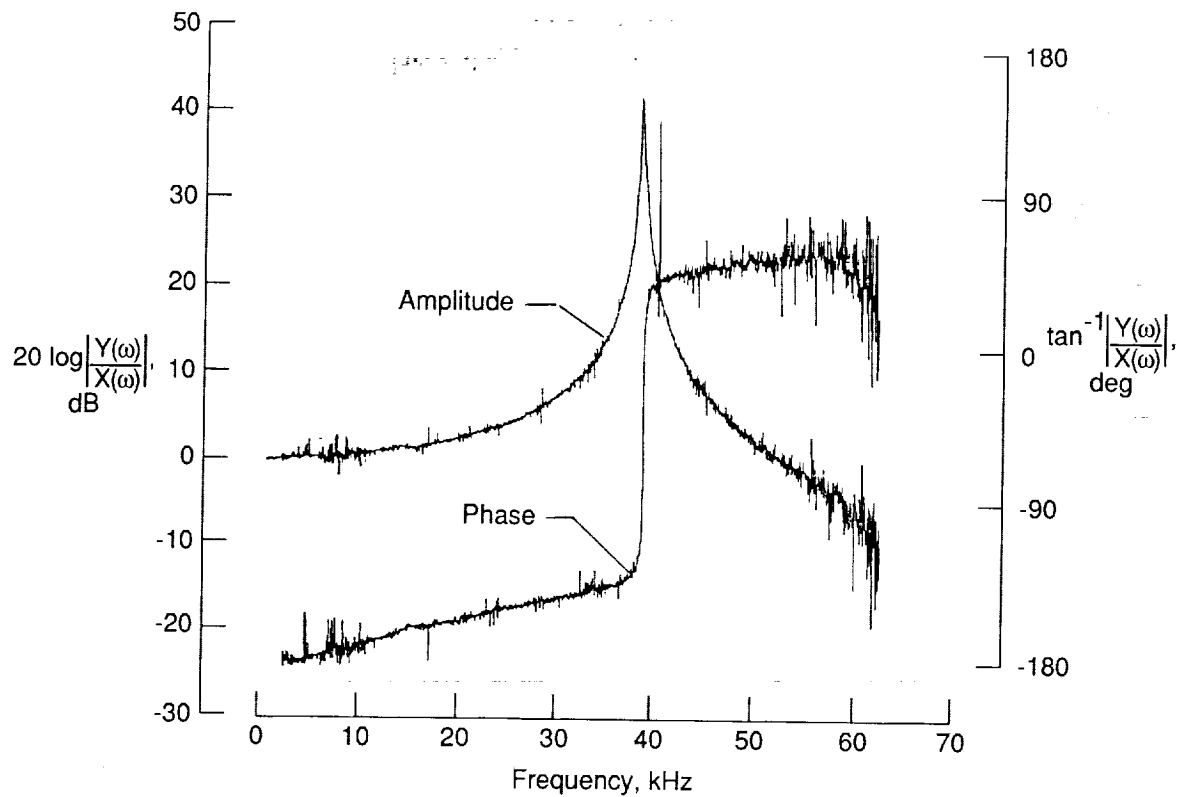


Figure 9. Typical transfer function of installed pressure sensor.

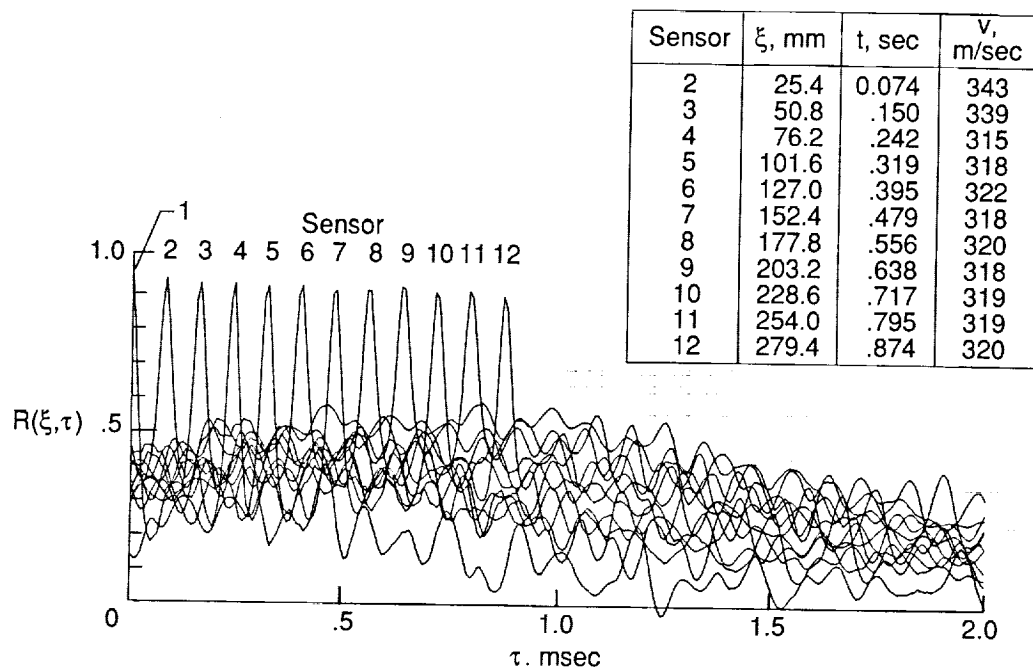
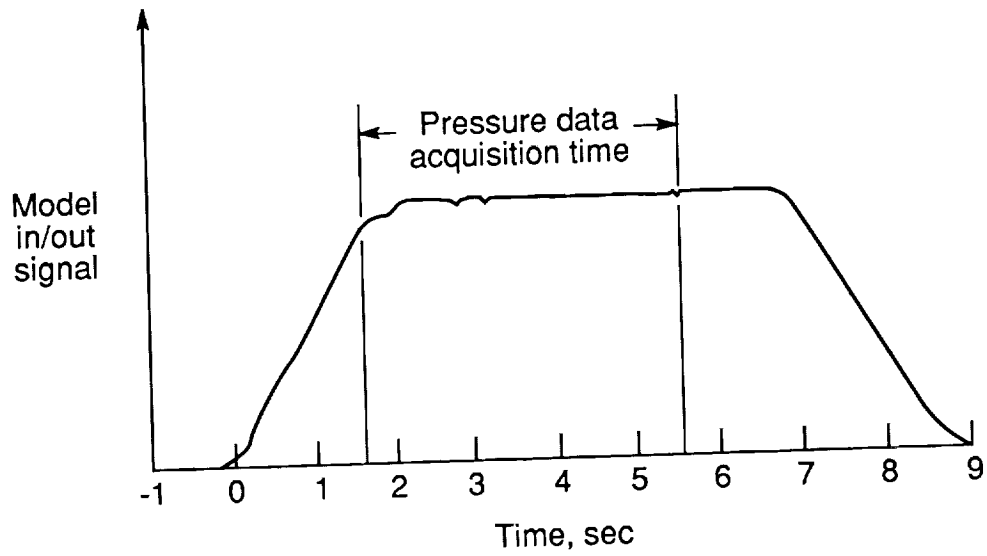
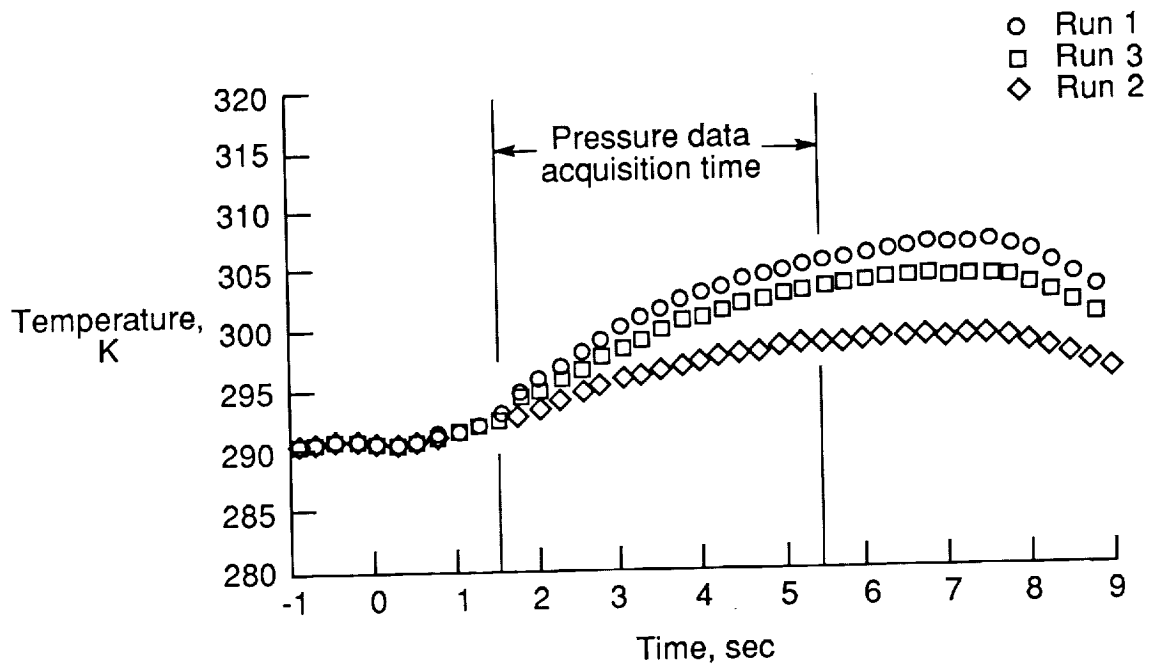


Figure 10. Space-time correlations for sensors installed in waveguide with air as propagating medium.



(a) Voltage signal proportional to model position during a typical run.



(b) Temperature time histories obtained from thermocouple located on array plate.

Figure 11. Surface temperature time histories and acquisition time for corresponding surface pressure data.

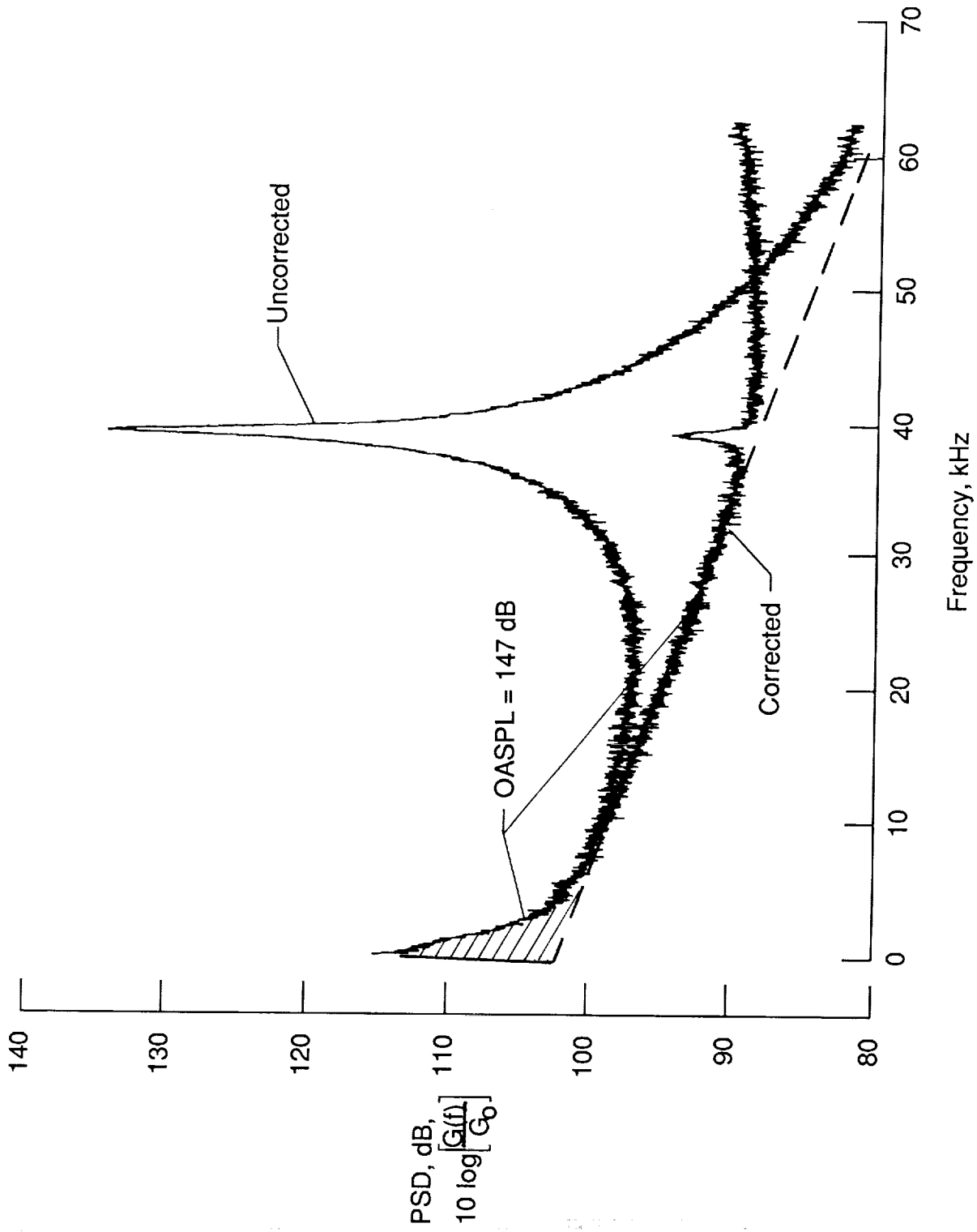
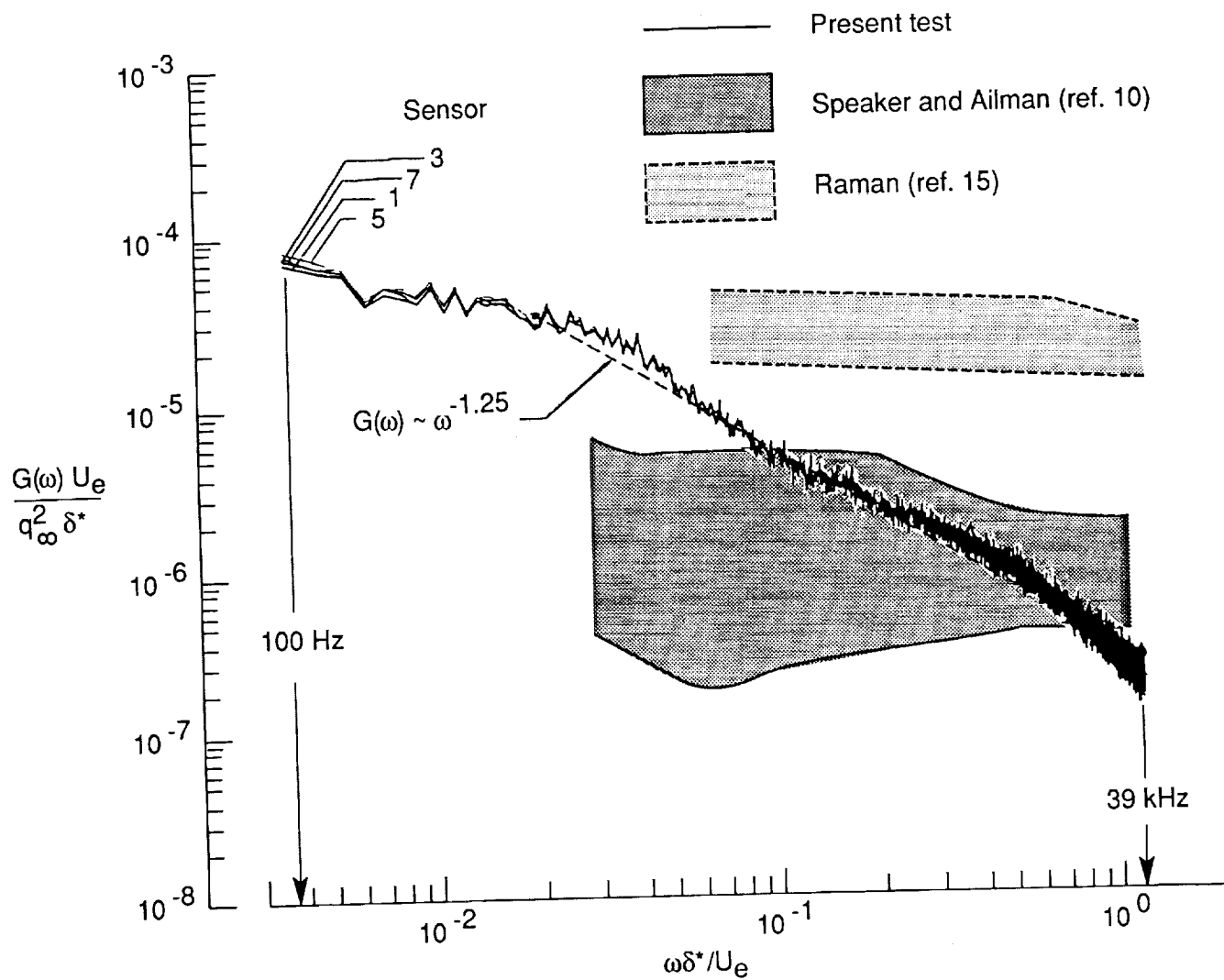
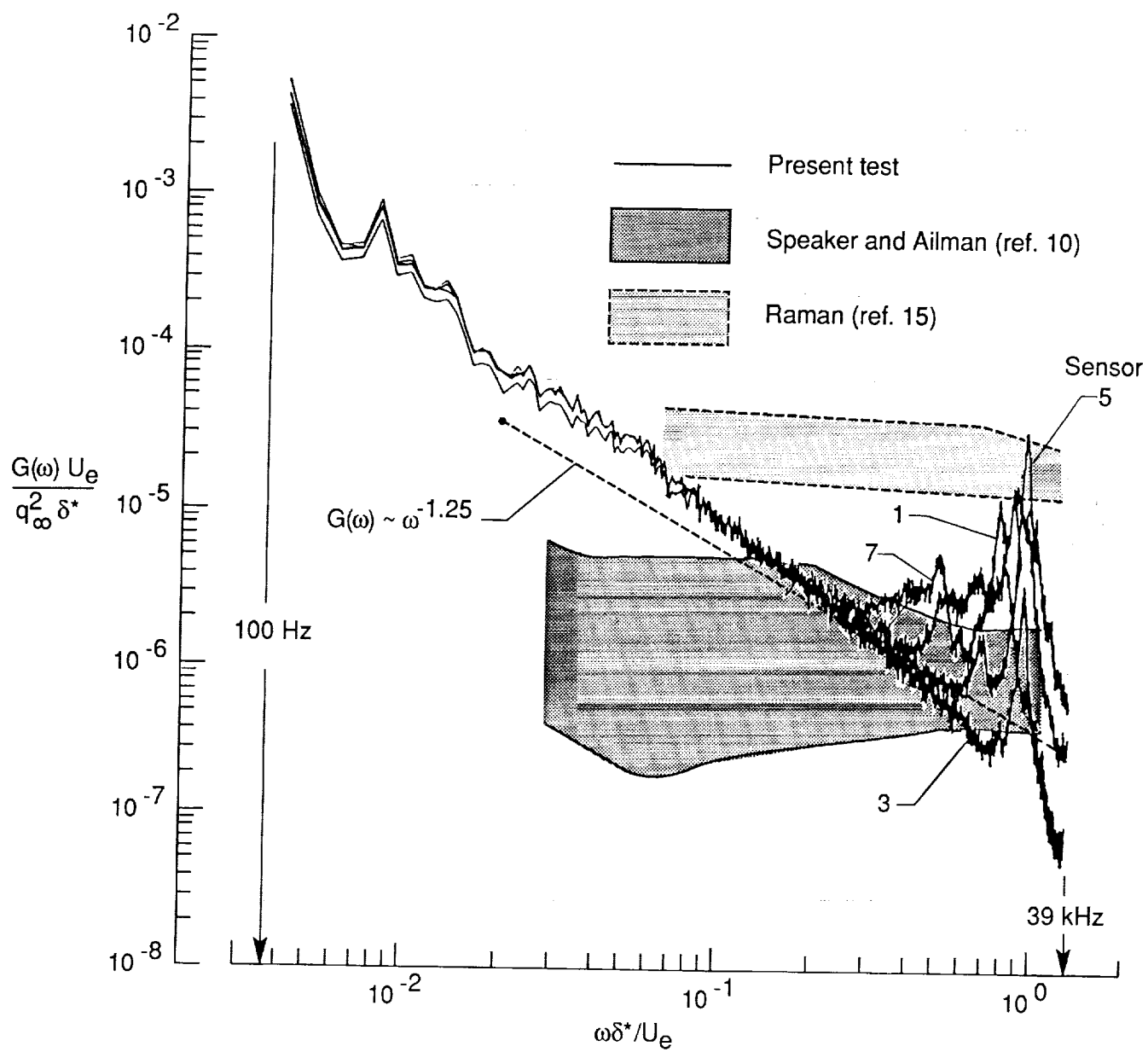


Figure 12. Power spectrum measured at sensor 1. Run 1; $N_{Re,\delta^*} = 100 \times 10^3$; extrapolated data (OASPL = 143 dB) are indicated by the dashed-line curve.



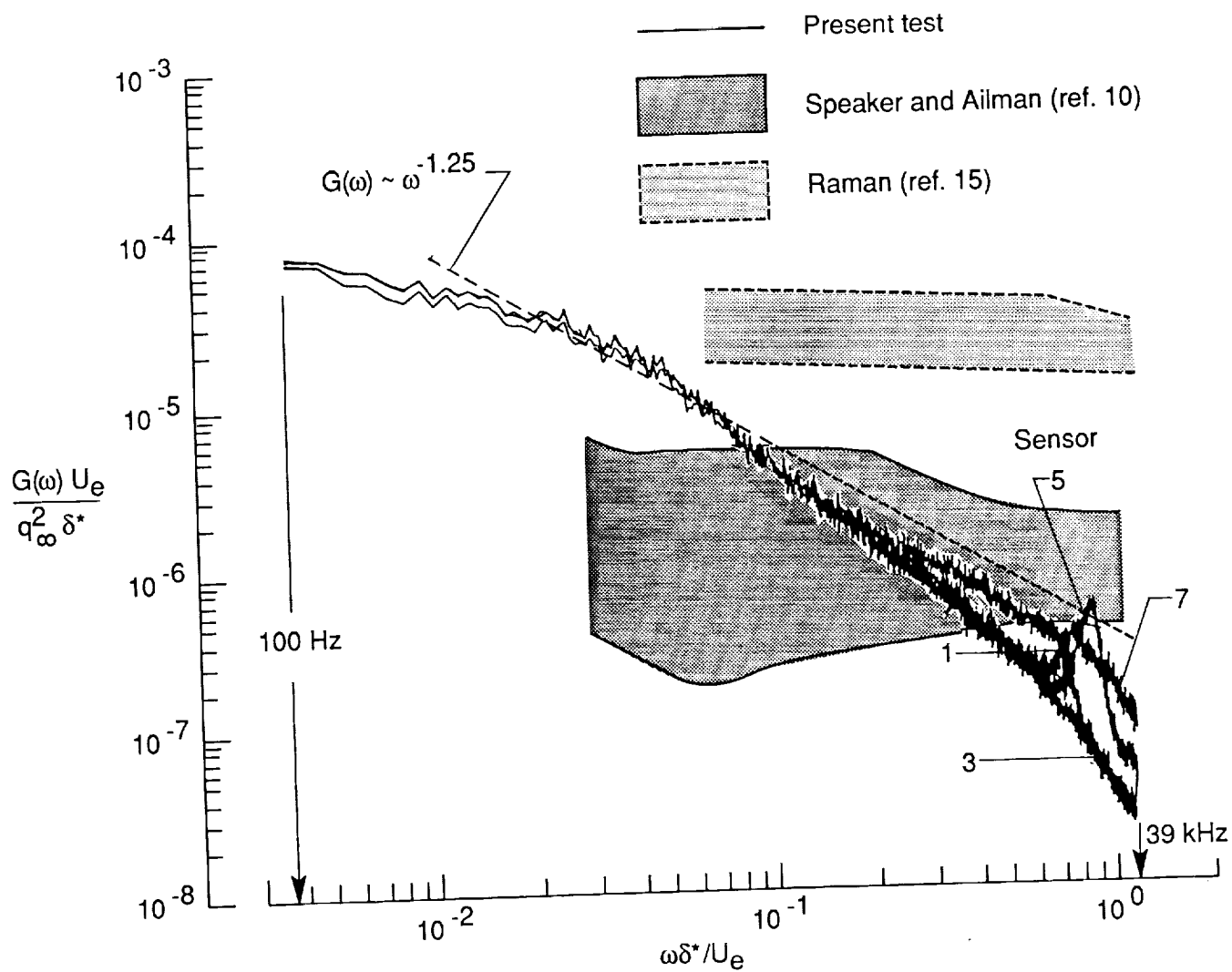
(a) Run 1; $N_{Re, \delta^*} = 100 \times 10^3$.

Figure 13. Comparison of normalized pressure spectra for streamwise sensors.



(b) Run 2; $N_{Re, \delta^*} = 44.2 \times 10^3$.

Figure 13. Continued.



(c) Run 3; $N_{Re, \delta^*} = 76.2 \times 10^3$.

Figure 13. Concluded.

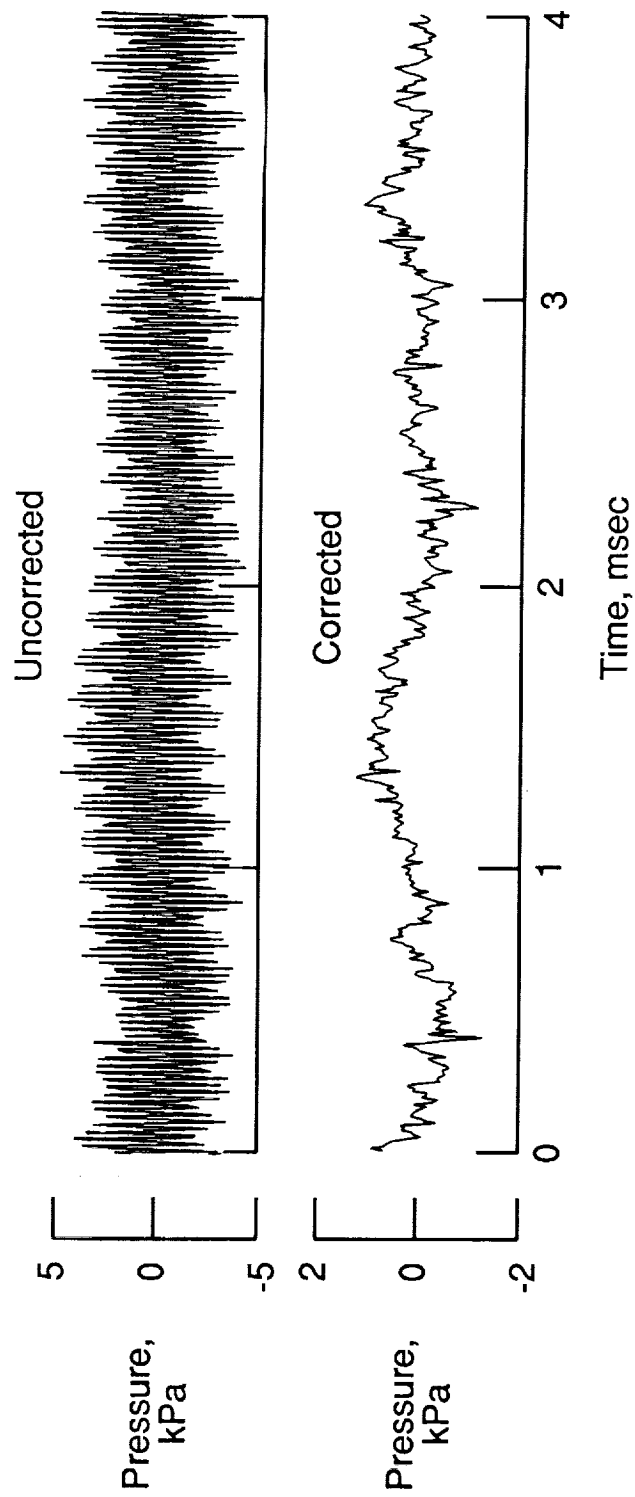
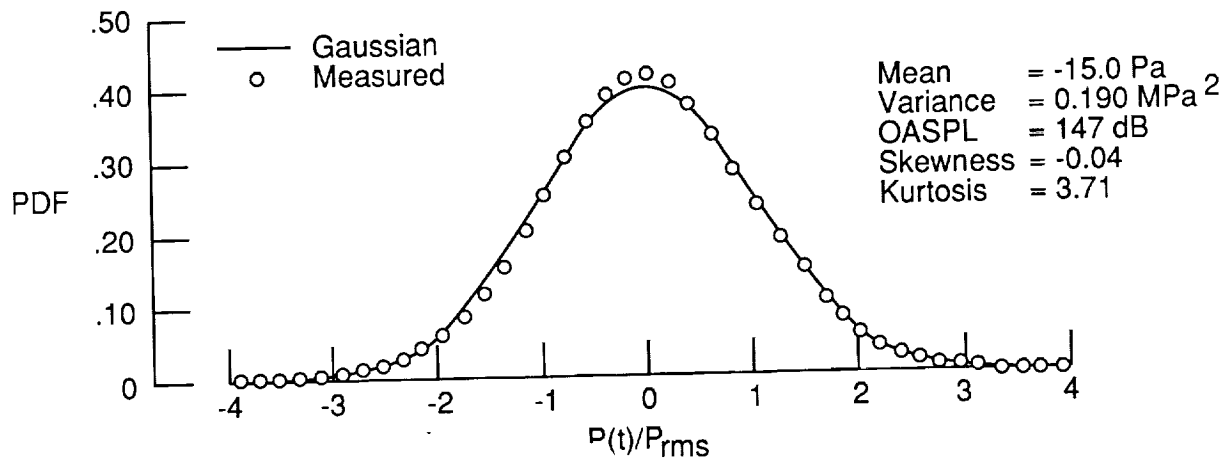
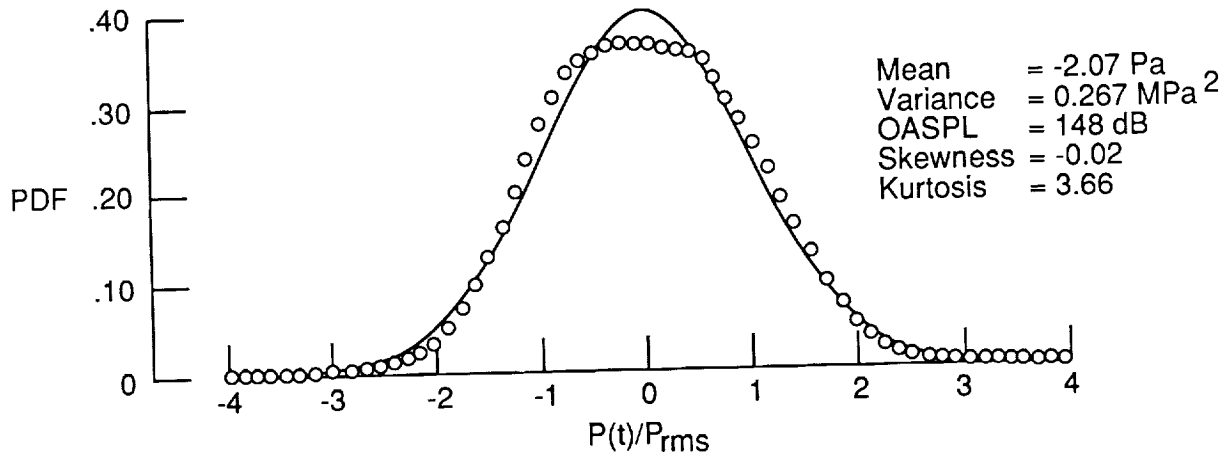


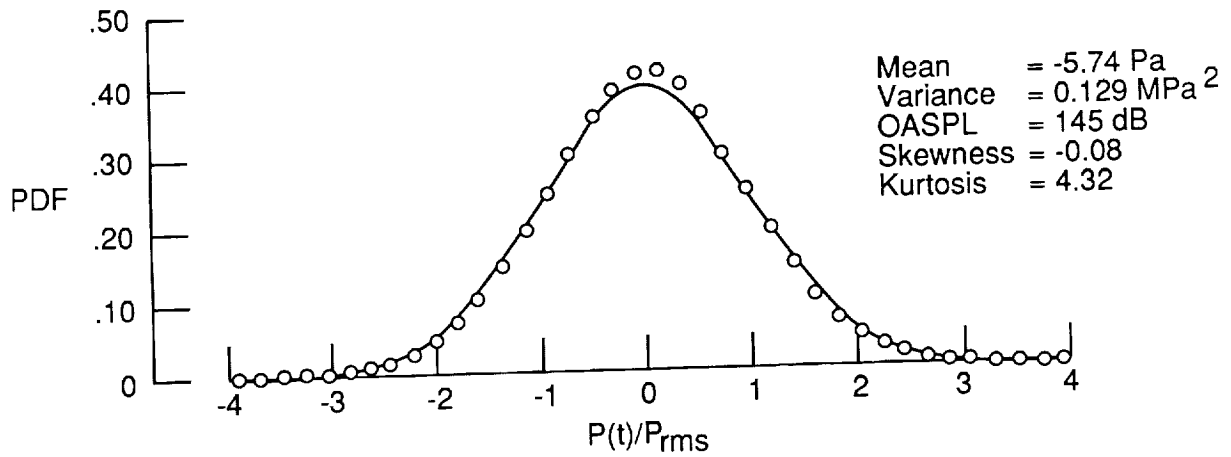
Figure 14. Example from run 1 of resonance-correction algorithm operating on measured time history at sensor 1.



(a) Run 1; $N_{Re,\delta^*} = 100 \times 10^3$.



(b) Run 2; $N_{Re,\delta^*} = 44.4 \times 10^3$.



(c) Run 3; $N_{Re,\delta^*} = 76.2 \times 10^3$.

Figure 15. Probability density distribution of pressure time histories measured at sensor location 1.

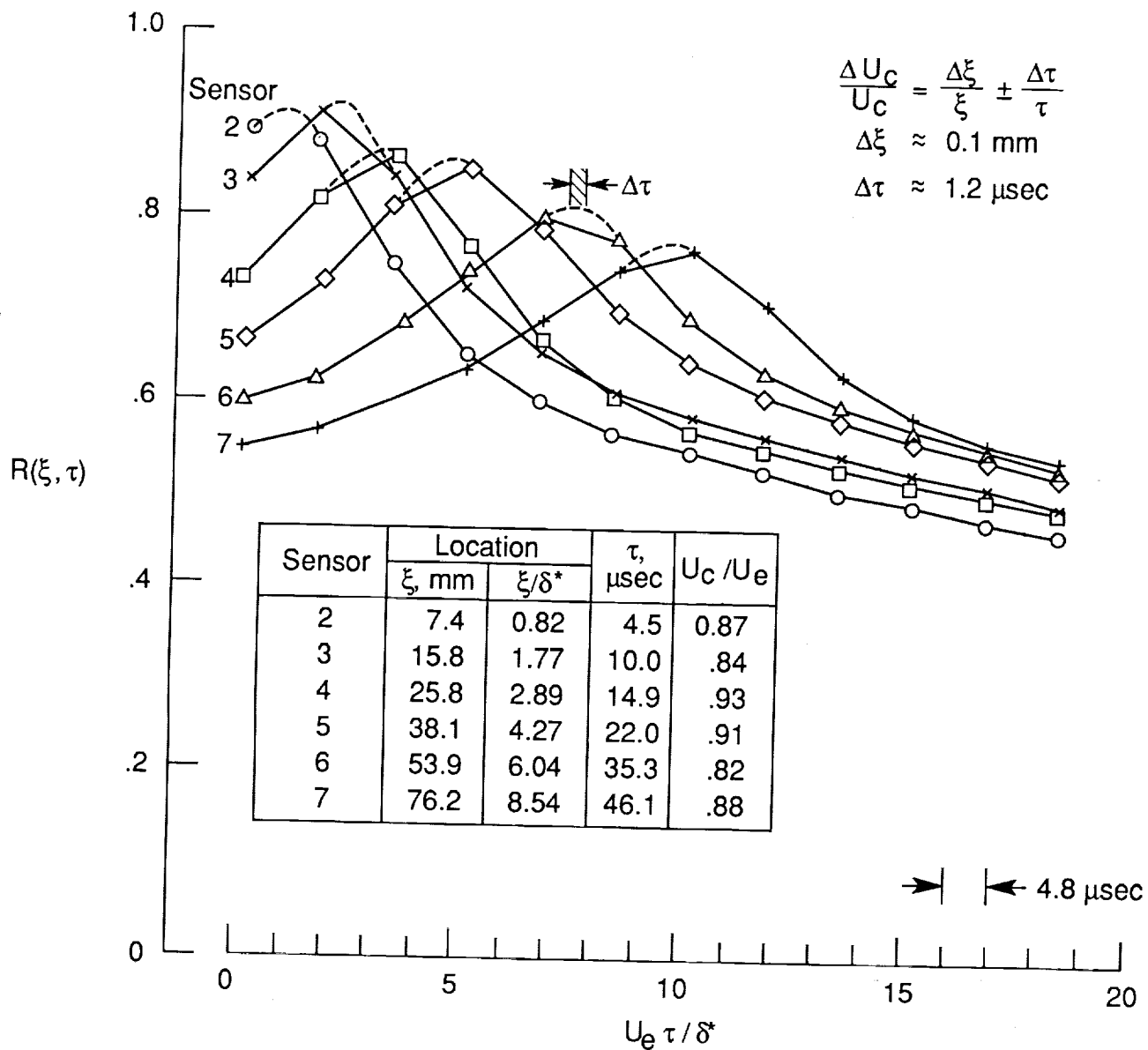


Figure 16. Space-time correlations in streamwise direction for $N_{Re, \delta^*} = 100 \times 10^3$.

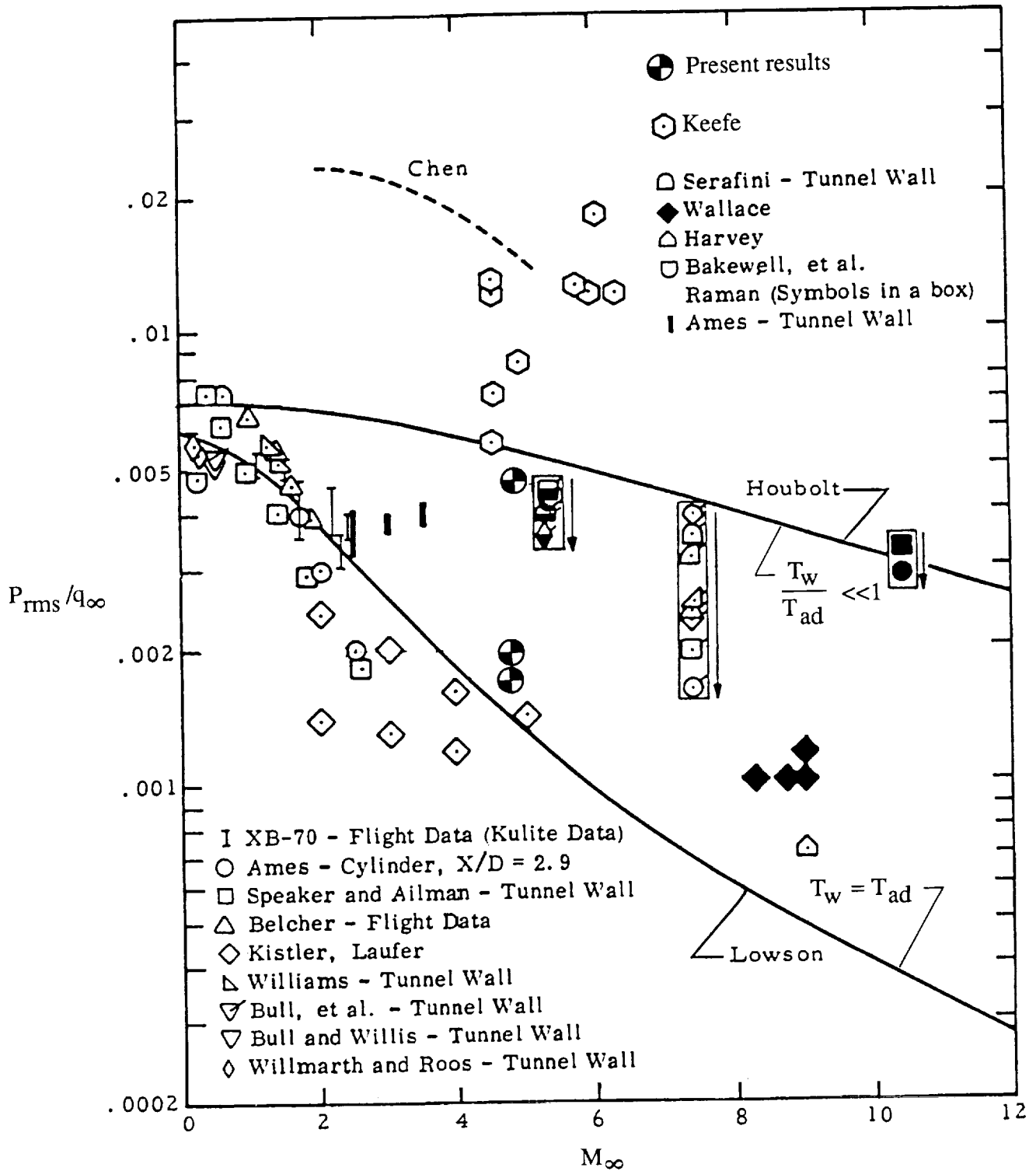


Figure 17. Ratio of RMS pressure to dynamic pressure plotted against free-stream Mach number. Present results and Keefe's data are compared with previous results originally presented in figure 28 of reference 15 by Raman.

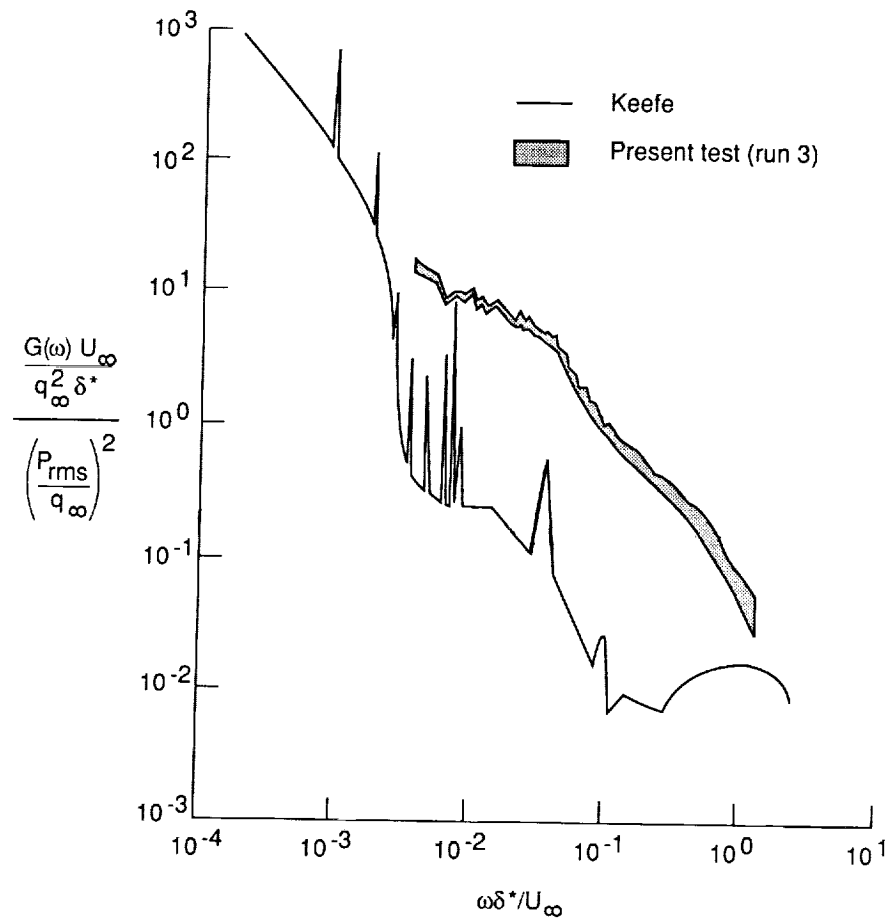


Figure 18. Comparison of pressure spectrum from previous test with that of present test.

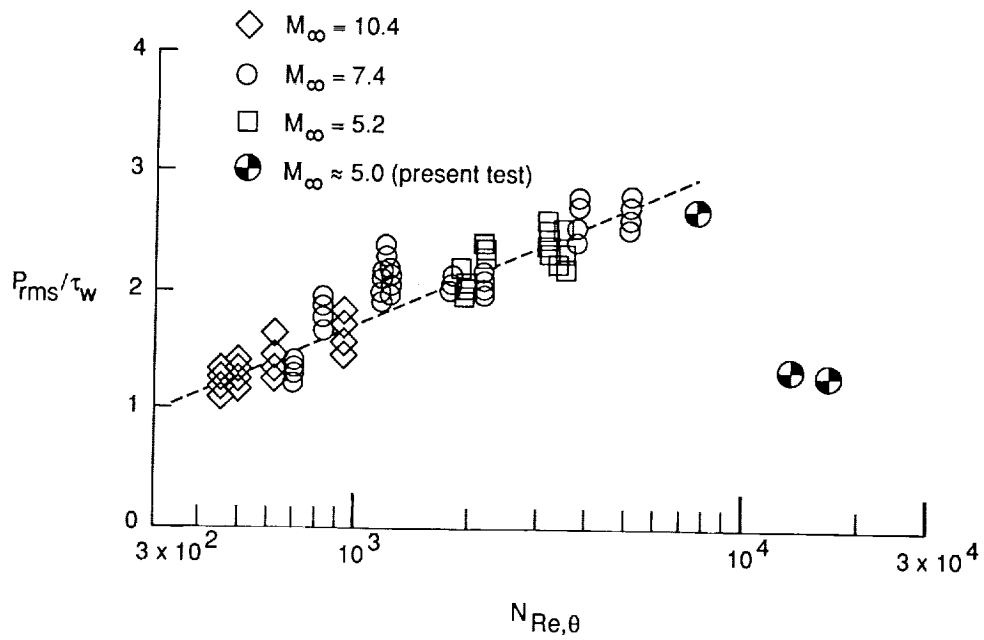


Figure 19. Present results for P_{rms}/τ_w versus $N_{Re,\theta}$ are compared with those of reference 15 by Raman.

1. Report No. NASA TP-2947		2. Government Accession No.		3. Recipient's Catalog No.	
4. Title and Subtitle Fluctuating Pressures Measured Beneath a High-Temperature, Turbulent Boundary Layer on a Flat Plate at a Mach Number of 5				5. Report Date November 1989	
				6. Performing Organization Code	
7. Author(s) Tony L. Parrott, Michael G. Jones, and Cindy W. Albertson				8. Performing Organization Report No. L-16596	
				10. Work Unit No. 506-80-31-06	
9. Performing Organization Name and Address NASA Langley Research Center Hampton, VA 23665-5225				11. Contract or Grant No.	
				13. Type of Report and Period Covered Technical Paper	
12. Sponsoring Agency Name and Address National Aeronautics and Space Administration Washington, DC 20546-0001				14. Sponsoring Agency Code	
15. Supplementary Notes Tony L. Parrott and Cindy W. Albertson: Langley Research Center, Hampton, Virginia. Michael G. Jones: PRC Kentron, Inc., Aerospace Technologies Division, Hampton, Virginia.					
16. Abstract Fluctuating pressures were measured at a Mach number of 5 beneath a turbulent boundary layer on a flat plate with an array of piezoresistive sensors. The data were obtained with a digital signal acquisition system during a test run of 4 sec. The data sampling rate was such that the frequency analysis could be performed up to 62.5 kHz. To assess in situ frequency response of sensors, a specially designed waveguide calibration system was employed to measure transfer functions of all sensors and related instrumentation. Pressure time histories were approximated well by a Gaussian-probability distribution. Pressure spectra were very repeatable over the array span of 76 mm. Total root-mean-square pressures ranged from 0.0018 to 0.0048 of the free-stream dynamic pressure. Streamwise, space-time correlations exhibited expected decaying behavior of a turbulence-generated pressure field. The average convection speed was 0.87 of the free-stream velocity. The trendless behavior with sensor separation indicated possible systematic errors.					
17. Key Words (Suggested by Authors(s)) Boundary layer Hypersonic Turbulent In situ sensor calibration Pressure spectra High temperature				18. Distribution Statement Unclassified-Unlimited Subject Category 71	
19. Security Classif. (of this report) Unclassified		20. Security Classif. (of this page) Unclassified		21. No. of Pages 37	
				22. Price A03	

